Global and Planetary Change 211 (2022) 103791

Contents lists available at ScienceDirect

Global and Planetary Change

journal homepage: www.elsevier.com/locate/gloplacha

ITCZ precipitation and cloud cover excursions control *Cedrela nebulosa* tree-ring oxygen and carbon isotopes in the northwestern Amazon

Danny Vargas [a,*], Darwin Pucha-Cofrep [b], Sheila Serrano-Vincenti [c], Angélica Burneo [b], Lisseth Carlosama [c], Madison Herrera [c], Marco Cerna [d], Mihály Molnár [a], A.J. Timothy Jull [a,e,f], Marjan Temovski [a], Elemér László [a], István Futó [a], Anikó Horváth [a], László Palcsu [a]

[a] Isotope Climatology and Environmental Research Centre, Institute for Nuclear Research, Debrecen H-4026, Hungary
[b] Universidad Nacional de Loja, Carrera de Ingeniería Forestal, Laboratorio de Dendrocronología, EC-110101 Loja, Ecuador
[c] Universidad Politécnica Salesiana, Carrera de Ingeniería Ambiental, Grupo de Investigación en Ciencias Ambientales GRICAM, Centro de Investigación en Modelamiento Ambiental CIMA UPS, 170109 Quito, Ecuador
[d] Universidad Politécnica Salesiana, Carrera de Ingeniería en Biotecnología, Grupo de Investigación Nunkui Wakan, 170801 Quito, Ecuador
[e] Department of Geosciences, University of Arizona, Tucson, AZ 85721, USA
[f] University of Arizona AMS Laboratory, Tucson, AZ 85721, USA

ARTICLE INFO

Editor: Jed O Kaplan

Keywords:
ITCZ
SAMS
Tree-rings
Stable isotopes
Cedrela nebulosa
Radiocarbon
Dendroclimatology

ABSTRACT

The lack of delimitation between the South American Monsoon System (SAMS) and the Intertropical Convergence Zone (ITCZ) has led to problematic calibration of archives in paleoclimate studies, particularly in northern South America. We show for the first time recorded in a paleoclimate archive that the ITCZ is the primary controller of oxygen ($\delta^{18}O_{TR}$) and carbon ($\delta^{13}C_{TR}$) isotopes in *Cedrela nebulosa* tree-rings (1864–2018). In contrast, a monsoonal pattern is not observed at this latitude. Spatial correlations revealed that $\delta^{18}O_{TR}$ better reflects months of higher precipitation (Mar–Jun) in the western Amazon than local rainout processes at decadal time scale, owing to the strong convection in the basin at this time of the year. Similarly, this study identified cloud cover as a vital controller in sunshine duration, which influences the phenology of *Cedrela nebulosa*. We interpret the variability of the $\delta^{13}C_{TR}$ as an enhancement in the photosynthetic rate during light-increased months (Jul–Sep), strongly regulated by cloudiness reduction when the ITCZ rain band retreats to northwestern South America in austral winter. Overall, these results reveal that *Cedrela nebulosa* is well-adapted to wet environments, and its cellulose-based stable isotopic signals reflect the direct influence of the ITCZ excursions from austral autumn to winter (Mar–Sep) with minimal SAMS control.

1. Introduction

The complexity of South American climates is due to geographical position, extensive territory, distance from the oceans, and Andean topographic variability (Garreaud et al., 2009). Two major climate systems control the rainfall seasonality on the continent and correspond to the Intertropical Convergence Zone (ITCZ) and the South American Monsoon System (SAMS). These have been fundamental for interpreting new paleoclimate records (Baker and Fritz, 2015; Garreaud et al., 2009; Marengo et al., 2012; Zhou and Lau, 1998). Unfortunately, the delayed recognition of SAMS as monsoon has led to some confusion with the ITCZ in the climatological literature. The terms have been used interchangeably in some cases; however, their spatiotemporal characteristics are quite different (Vuille et al., 2012). Although the SAMS controls a significant part of the seasonal precipitation variability, its influence is limited to 10° away from the equator, because at latitudes between 10°N-10°S, the annual mean wind and velocity potential fields are approximately symmetric and do not reflect any monsoonal character (Chao and Chen, 2001; Douville et al., 2021; Murakami and Nakazawa, 1985). On the contrary, the ITCZ has been defined as a tropical belt of deep convective clouds where heat and moisture-laden surface trade winds converge, forming a zone of increased precipitation (Schneider et al., 2014; Waliser and Jiang, 2015). During the year at this tropical belt, the ITCZ undergoes two latitudinal excursions which follow the regions of warmest sea surface temperature (SST) and seldom moves far from the equator, as a result of the ocean's thermal inertia (Vuille et al.,

* Corresponding author at: Debrecen, P.O. BOX 51, H-4001, Hungary.
E-mail address: danny.vargas@atomki.hu (D. Vargas).

https://doi.org/10.1016/j.gloplacha.2022.103791
Received 2 April 2021; Received in revised form 6 March 2022; Accepted 16 March 2022
Available online 19 March 2022

2012; Xian and Miller, 2008). Globally, the rainfall belt has two migrations from the southern (SH) to the northern hemisphere (NH). One occurs in April (day 100) and the other in December (day 345). The transition from the SH to NH in April is smooth, contrary to the abrupt shift from NH to SH in December caused by a larger ground thermal inertia (Hu et al., 2007; Xian and Miller, 2008). In South America, the ITCZ reaches its maximum NH latitude in July (boreal summer) and highest SH latitude in January (austral summer) at 10°N and 5°S respectively, playing a crucial role in the moisture influx, especially in northern South America (García, 1994; Garreaud et al., 2009; Hastenrath, 1997).

Previous paleoclimate studies in northwestern South America have not dealt with the distinction between the ITCZ and SAMS as drivers of rainfall seasonality. Variations in the precipitation oxygen isotope signal ($\delta^{18}O_{prec}$), particularly in speleothems, have been placed mainly into the SAMS context (Cheng et al., 2013; Mosblech et al., 2012), although the ITCZ and SAMS are well studied (Garreaud et al., 2009; Vuille et al., 2012; Wang et al., 2013; Zhou and Lau, 1998). Regionally, the climate of Ecuador is an interesting case study. Crossing the equator and located in both hemispheres, the country is influenced by modes of precipitation variability occurring in Colombia and Peru. For these latter countries, the rainfall seasonality responds to the ITCZ and SAMS, respectively, making Ecuador a transition zone between these climatic systems (Garreaud et al., 2009; Ilbay-Yupa et al., 2021; Poveda et al., 2006; Wang and Fu, 2002). Few studies have systematically investigated the ITCZ and SAMS actual boundaries, which has been amplified by climate data shortcomings and the lack of extended local records of $\delta^{18}O_{prec}$ in the country (Vuille et al., 2012). This difficulty has been exposed by Villacís et al. (2008) regarding the lack of $\delta^{18}O_{prec}$ monitoring needed for reliable calibration of an ice core drilled from the Chimborazo glacier (6268 m, 1°30′S, 78°36′W) because the precipitation over northern tropical South America is usually underestimated by Atmospheric General Circulation Models (Vuille et al., 2003).

Similarly, a 94 ka BP speleothem-based precipitation reconstruction from the Santiago cave in the Ecuadorian Amazon was interpreted based on moisture transported by the South American low-level jet (a SAMS mesoscale process) driven by the Atlantic Sea surface temperature (SST). At the same time, the climatic inferences were derived from regional models (Mosblech et al., 2012). Furthermore, in their recent work, Montoya et al. (2018) obtained paleolimnological data from Laguna Pindo (1250 m a.s.l.) in central Ecuador, spanning the last glacial period (50–13 ka BP) and used as a paleoclimatic background an independent Greenland ice core archive for calibrating temperature along with the aforementioned Santiago speleothem record to assess precipitation. Overall, these studies indicate that the dynamics of the ITCZ and SAMS are well understood (Garreaud et al., 2009; Vuille et al., 2012). However, the evidence for their demarcation has not been examined with terrestrial archives; hence ambiguity still exists for paleoclimate studies in Ecuador.

In stable isotope dendroclimatology, where trees uptake soil water dominated by precipitation, the water has an isotopic signature related to local air-mass characteristics carrying a specific atmospheric ^{18}O imprint. Hence, it is assumed that the obtained oxygen isotopic signal in tree-rings ($\delta^{18}O_{TR}$) will mainly reflect the $\delta^{18}O_{prec}$ (Loader et al., 2007; McCarroll and Loader, 2004; Treydte et al., 2014). In tropical regions, $\delta^{18}O_{TR}$ has been primarily used as a proxy for reconstructing past precipitation and identifying annual rings in ring-less wood (Baker et al., 2016; Brienen et al., 2012; van der Sleen et al., 2017). As a complement to $\delta^{18}O_{TR}$, carbon isotopes in tree-rings ($\delta^{13}C_{TR}$) have been shown to reflect changes in the internal concentration of CO_2 (c_i) within the leaf space compared to ambient CO_2 (c_a) (McCarroll and Loader, 2004). The amount of CO_2 in leaves is actively regulated by the stomatal conductance (g) and photosynthetic rate (A). The climatic controls regulating A are irradiance (light availability) and temperature. For g, air humidity and soil moisture are the main signal controls (Loader et al., 2007; van der Sleen et al., 2017). Usually, $\delta^{13}C_{TR}$ is expressed relative to a pre-industrial standard value by adding a correction factor. This value corrects the atmospheric decline in the atmospheric $\delta^{13}C$ signal due to an increase in c_a of anthropogenic origin (McCarroll and Loader, 2004).

Several dendroclimatological studies employing $\delta^{18}O_{TR}$ have recently contributed to counteract the sparsity of climate data in Ecuador, and *Cedrela* (Meliaceae) has been the preferred genus due to its diversification, spread, and annual ring formation (Pennington and Muellner, 2010). The records primarily come from two montane Andean forests of *Cedrela montana* from southern Podocarpus National Park (PNP) (1885–2011, 1800–3180 m a.s.l.) and northern Cuyuja (1799–2012, 2950 m a.s.l.) shown in Fig. 1 (Baker et al., 2018; Volland et al., 2015). The meridional PNP $\delta^{18}O_{TR}$ record has shown positive correlations with seasonal precipitation from January to April, frequency of wet days, and cloud cover over the Andean Cordillera Real. Spatially it has given strong correlations with the El Niño-Southern Oscillation (ENSO), which influences its $\delta^{18}O_{TR}$. On the other hand, $\delta^{18}O_{TR}$ from Cuyuja resulted in a good proxy for studying the Amazon hydro-climatic variability in the past centuries. The observed change in the $\delta^{18}O_{TR}$ trend was interpreted as a reduction in rainout fraction over the Amazon basin, probably driven by the warming of the Sea Surface Temperature (SST) in the North Atlantic (Baker, 2017). These studies of $\delta^{18}O_{TR}$ have indicated direct Pacific and Atlantic Oceanic influence, respectively. However, the influence of either the ITCZ or the SAMS controlling the isotopic signals feeding the forests has not been evaluated thoroughly.

This paper aims to clarify the leading regional controller of climate variability in the Ecuadorian territory, focusing on the primary precipitation systems, ITCZ and SAMS, influencing South America using dendrochronological methods. For this purpose, tree-ring width (TRW), $\delta^{18}O_{TR,}$ and $\delta^{13}C_{TR}$ chronologies are constructed using *Cedrela nebulosa* T.D.Penn. & A. Daza trees from the Mera site in central Ecuador, which is a transition country between these rainfall systems.

2. Materials and methods

2.1. Study site

The study area is located in Mera, Province of Pastaza (1°24′S, 78°03′W, 1200 m a.s.l.) in the eastern foothills of the Ecuadorian Andes. The forest is locally classified as an evergreen piedmont forest over limestone outcrops of the Amazonian Cordillera (Neill and Guevara, 2013). The site is distinctive since it is a transition zone from the Amazon lowlands to the Andes with elevations above 4000 m a.s.l. (Fig. 1a). This latter has a significant influence on the regular moisture transport due to its role as an orographic barrier that enhances condensation and, therefore, precipitation making this site perhumid (Ilbay-Yupa et al., 2021; Insel et al., 2010). In fact, the mean annual rainfall for Puyo (1965–2018) and Shell (1981–2018) stations was 4586 and 5357 mm, respectively. The rainfall regime has been described as bimodal and consists of two minor (Dec-Feb and Jul-Sep) and two main rainy seasons (Apr-Jun and Oct-Nov) (Ilbay-Yupa et al., 2021) (Fig. 1b). It is noteworthy to mention that these thresholds serve as a reference, and sometimes the seasons may be shorter or longer, but the bimodality is preserved. On the other hand, the mean monthly temperature is steady and fluctuates between 21 and 23 °C during the year. Nevertheless, the months with the lowest temperature are from June to August, where the mean temperature drops to values below 21.0 °C (Fig. 1c). The mean annual temperature for Puyo (1965–2018) and Shell (1981–2018) was 21.7 °C and 22.4 °C, respectively.

2.2. Sampling and tree-ring identification

Initially, a field campaign in February 2019 was undertaken for identifying potential species for dendroclimatic purposes, considering the local forest heterogeneity. Transects were marked, extending a rope 50 m long and measuring 2.5 m on each side in a zigzag pattern covering

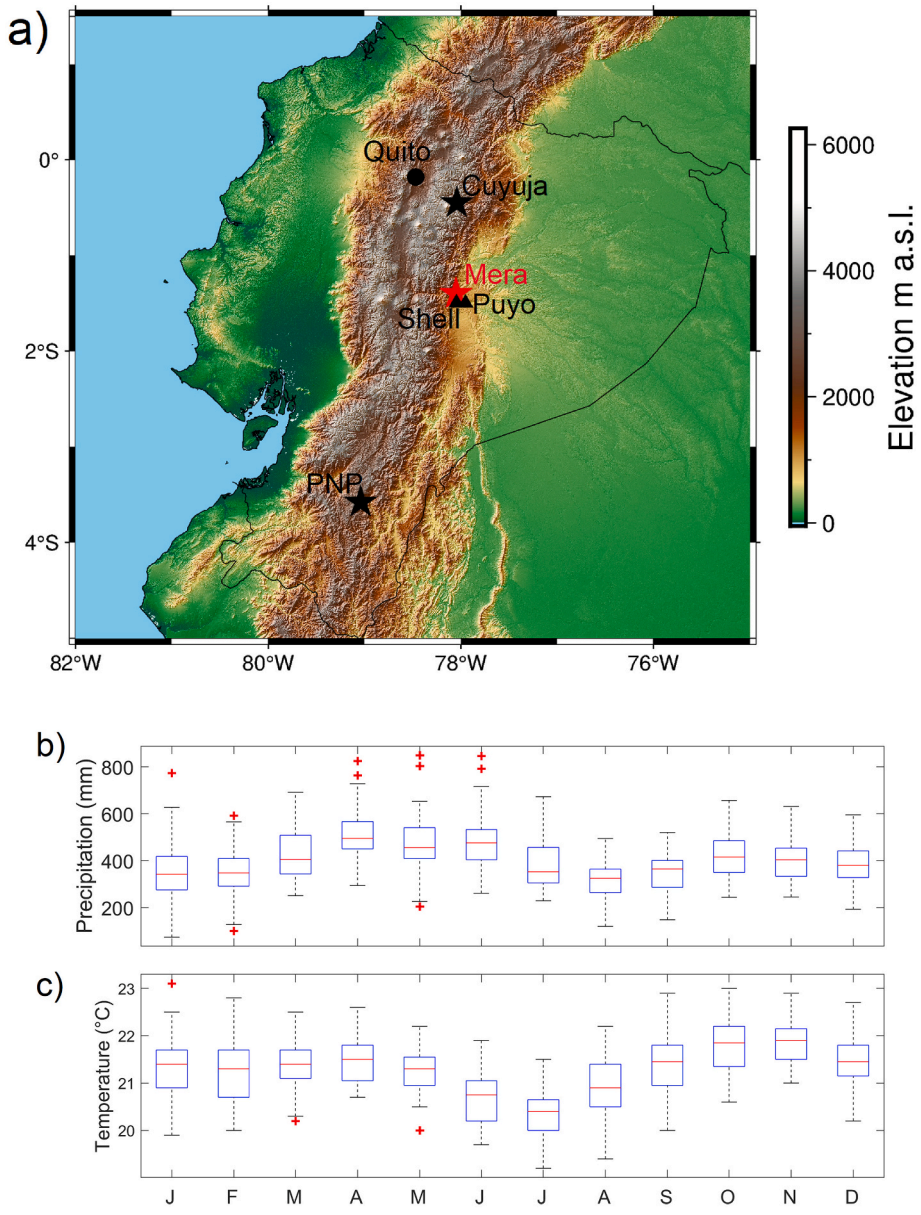

Fig. 1. (a) Location of the Mera study site (red star) positioned in the eastern Andean foothills (northwestern Amazon basin), central Ecuador. Previous study sites where $\delta^{18}O_{TR}$ chronologies have been constructed using *Cedrela montana* (Cuyuja and Podocarpus National Park PNP) are marked by a black star. The instrumental stations Shell (1°29′S, 78°02′W, 1043 m a.s.l.) and Puyo (1°30′S, 77°57′W; 956 m a.s.l.) are located 10 and 15 km away from the study site and are shown in black triangles. Climographs of monthly (b) precipitation and (c) temperature averaged between the instrumental stations (1965–2018). Boxplots show the location of the middle quartile of monthly observations with their median (horizontal red line). The whiskers extend to the two extreme data values. Outliers are any data value more than 1.5*IQR, where IQR is the interquartile range (red cross marker). Datasets correspond to the National Institute of Meteorology and Hydrology (INAMHI) and the Civil Aviation Directorate (DAC). (For interpretation of the references to colour in this figure legend, the reader is referred to the web version of this article.)

a total area of 250 m^2 (Cámara Artigas and Díaz del Olmo, 2013). The process was repeated until eight transects were completed (2000 m^2 = 0.2 ha). Areas with steep slopes and with visible traces of human transit were avoided since these were indicators of possible forestry logging, thus reducing the probability of finding long-lived trees (Stahle, 1999). Along to the marked transects, increment cores were extracted at breast height (1.3 m) using a Haglöf 5 mm Pressler borer. In addition, botanical samples with their corresponding reproductive organs (flowers and fruits) were collected for taxonomic identification following standard protocols (Engelmann, 1986). Botanical samples were dried at 60 °C for 48 h in a BINDER FD 23–20 L drying chamber and identified at the following Herbariums: Universidad Nacional de Loja-Reinaldo Espinoza, Universidad Central del Ecuador-Alfredo Paredes (QAP), and National Herbarium of Ecuador (QCNE). Finally, Simpson's (dominance and abundance) and Shannon's abundance landscape diversity indices were calculated (see Supplementary Fig. S1). The *Cedrela nebulosa* species was the most appropriate from all collected specimens due to its prominence and visible rings display. Unfortunately, this species is a deciduous broad-leaved tree in a current vulnerable status (CITES, (Convention on International Trade in Endangered Species of Wild Fauna and Flora), 2021; Tropicos.org, 2020). Hence, in a second field campaign in September 2019 to improve the dating in tree-rings, four cores per tree were collected in the four cross directions of the trunk (total 33 trees, 67 radii, and 3 cross-sections). The increment cores were mounted in wooden grooved holders with the direction of vessels vertically aligned and air-dried in the laboratory. Then, the cores were consecutively sanded up to 4000 grit enhancing tree-ring visibility (Stokes and Smiley, 1968).

Tree-ring width measurements were carried out in the Laboratorio de Dendrocronología at the Universidad Nacional de Loja using a LINTAB 6 measuring system (Rinntech, Heidelberg, Germany) with a 0.01 mm precision coupled with TSAP-Win software (Rinn, 2012). For cross-dating, a visual inspection of tree-ring patterns and standard statistical tests were performed (Cook et al., 1990). TRW series from stem disks were used to reference the synchronization of individual series from increment cores. Every tree-ring series was checked visually and statistically for cross-dating quality. Some series were excluded from the chronology based on ring-boundary visibility, wood damage, the occurrence of missing or wedging rings, and recurrent cross-dating problems, leaving 24 trees for subsequent work from the original 33

sampled on the field. All individual tree-ring series were grouped and saved in Heildelberg format (.fh), then imported to the R statistical programming environment (R Core Team, 2020). To analyze and evaluate the statistical quality of the cross-dated TRW series, the "Dendrochronology program library in R (dplR)" was used (Bunn, 2008). Individual growth tendencies related to age and natural effects were removed through a "detrending" procedure. Preliminary interactive assessment utilized the "detrendeR" package (Campelo et al., 2012), and the following work employed a non-interactive detrending in the "dplR" package with the "detrender ()" routine. From the obtained detrended series, chronologies were built with the "chron ()" function ("dplR" package), from which standard and residual chronologies were obtained. In this study, both chronologies were evaluated, but the standard chronology was used. In addition, the chronology was built with prewhitening and biweight in order to have a robust mean using the dplR package. The Expressed Population Signal (EPS) was calculated to obtain the similarity or common signal between several trees of the population, and it ranged from 0 to 1. Generally, an EPS of 0.85 is suggested to capture a common signal, while the remaining 0.15 is a residual chronological variance (Wigley et al., 1984). The EPS was computed using the chronology Stripping "strip.rwl ()" function, which selects the best time-series with the most similarity in each site (Bunn, 2010). In this study, the EPS was calculated using 24 trees for the TRW chronology.

2.3. Annual ring validation

Wood anatomical features and independent validation of annual ring formation using ^{14}C provided a solid basis for constructing TRW, $\delta^{18}O_{TR,}$ and $\delta^{13}C_{TR}$ chronologies. In the first case, wood thin sections of 10 to 20-μm thickness were prepared with a microtome, stained with safranin and astra blue solutions, and washed with ethanol (Gärtner and Schweingruber, 2013). Then, microscopic images were taken for ring boundary identification, vessel numbers, and diameter measurements.

After measuring the ring widths of all wood cores with subsequent cross-dating, 18 rings were selected in the region of the "bomb-peak" for ^{14}C measurements. Samples were prepared using a standard BABAB (basic-acid-basic-acid bleaching) α-cellulose method (Molnár et al., 2013a). Then, cellulose was combusted to CO_2 (550 °C, 12 h.) with MnO_2 as a reagent (Janovics et al., 2018). The resulting gas was purified on a vacuum line with a dry ice-isopropyl alcohol mixture and a liquid nitrogen trap. Finally, graphite was obtained through a sealed tube graphitization method (Rinyu et al., 2013) and ^{14}C measured by a MICADAS (mini carbon dating system) type AMS (Molnár et al., 2013b). The resulting percent modern carbon (pMC) values were isotope-fractionation corrected, expressed to fraction modern ($F^{14}C$), and compared with the post-bomb calibration curves for the Southern Hemisphere (SH Zone 1–2 and SH Zone 3) (Hua et al., 2013; Reimer and Reimer, 2004).

2.4. Tree-ring oxygen and carbon isotopes

Four dominant, long-lived, cross-dated tree cores were selected. We visually separated 1-year samples assisted by a Zeiss SteREO Discovery. V20 stereo microscope, and a scalpel. We measured each tree separately and averaged the results afterward, allowing us to account for intrasite variability and minimizing isotopic changes due to considerable growth variations in ring width (Borella et al., 1998). However, when rings were excessively narrow to separate conveniently, 2–3 consecutive rings were taken as one averaged sample to provide enough material for isotopic analysis. The obtained isotopic value in these sections was replicated in the neighboring rings to construct the individual chronology for each particular tree (Supplementary Dataset).

The preparation of α-cellulose was based on the method described by Túri et al. (2021), modified to suit tree-ring samples, and is briefly summarized here. Resin and other soluble materials from individual tree-rings were removed by solvent extraction using a mixture of chloroform and ethanol (2:1 ratio) for approximately 6 h. Then, lignin was oxidized using an acidified sodium chlorite solution in an ultrasonic bath at 70 °C, followed by the removal of hemicellulose in sodium hydroxide in an ultrasonic bath at 80 °C. Finally, samples were rinsed using deionized water and freeze-dried. Carbon and oxygen stable isotope ratio measurements were then carried out on the extracted cellulose samples. The stable isotopes were measured on a Thermo Scientific™ EA IsoLink™ IRMS System for CNSOH known as Flash EA, which is an enhanced elemental analyzer for oxygen and carbon isotope analyses as well. It is equipped with an automatic switching valve that allows fast switching from carbon analysis (Combustion) to oxygen analysis (Pyrolysis). Cellulose (0.25 ± 0.04 mg) was weighed into silver capsules for oxygen analysis and aluminium capsules for carbon analysis, then dropped into the autosampler of the elemental analyzer. The instrument is coupled to a Thermo Finnigan Delta^{PLUS} XP continuous-flow isotope ratio mass spectrometer. Results are expressed in conventional delta notation as follows, $\delta\ (\%) = (R_{sample}/R_{reference} - 1)$ *1000, where R is the $^{18}O/^{16}O$ or $^{13}C/^{12}C$ ratio of the sample or reference standard. The $\delta^{18}O$ and $\delta^{13}C$ values are relative to VSMOW and VPDB standards, respectively. For $\delta^{18}O$, the used standard materials were celluloses IAEA-C3 (+32.14‰, VSMOW) and Merck (+28.67‰, VSMOW), then benzoic acid IAEA-601 (+23.14‰, VSMOW) (Kéri et al., 2015; Saurer et al., 1998). For $\delta^{13}C$, the used reference materials were IAEA-C3 cellulose (−24.91‰, VPDB) and IAEA C-5 wood (−25.49‰, VPDB) then an in-house sulfanilamide standard (−26.69‰, VPDB). Every cellulose sample was measured at least twice for each stable isotope, and standard deviations of individual $\delta^{13}C$ and $\delta^{18}O$ measurements were ± 0.1‰ and ± 0.35‰, respectively.

In the case of Combustion, the analytical method is based on the complete and instantaneous oxidation of the sample by flash combustion at 1020 °C, which converts all cellulose substances into combustion products. The resulting combustion gases (in this case CO_2) are swept into the chromatographic column by the carrier gas (helium). The gases are separated in the column and detected by the mass spectrometer. For Pyrolysis (high-temperature conversion), the samples are pyrolytically decomposed in a high-temperature pyrolysis system at a temperature exceeding 1450 °C in the presence of reactive carbon. The resulting gases (in this case CO) are swept into the chromatographic column by the carrier gas (helium). The gases are separated in the column and detected by the mass spectrometer. Lastly, each $\delta^{13}C_{TR}$ measured value was adjusted by adding a correction factor (Δ) necessary to quote $\delta^{13}C_{TR}$ values relative to a pre-industrial standard value of −6.4‰ as recommended by McCarroll and Loader (2004). This correction addresses the atmospheric decline in $\delta^{13}C$ signal due to an anthropogenic increase in the CO_2 concentration in the atmosphere. The estimated annual values of atmospheric CO_2 (ppm) were obtained from McCarroll and Loader (2004) (Table 2) from 1864 to 2003 and then extended until 2018 from the Mauna Loa CO_2 records (Tans and Keeling, 2020).

2.5. Climate datasets

2.5.1. Partial correlations with growth rings

In our study, precipitation and temperature gridded datasets from the Climate Research Unit CRU TS4.04 with a horizontal resolution of 0.5° x 0.5° (Harris et al., 2020) were used as input to identify the seasonal climate signal in the TRW, $\delta^{18}O_{TR,}$ and $\delta^{13}C_{TR}$ chronologies. This analysis is consistently carried out using partial correlation analysis (Meko et al., 2011). Usually, a primary and a secondary climate variable are selected, being temperature and precipitation the most frequently employed. The relationship of the tree-ring series with the primary climate variable uses simple correlations. In contrast, the relationship with the secondary climate variable utilizes partial correlations, which controls the influence of the primary climate variable (Meko et al., 2011). The seascorr MATLAB package (Meko et al., 2011) was used for the partial correlation analysis at monthly resolution. The CRU TS4.04

gridded climate data was cropped using the shapefile from the National Institute of Statistics and Census (INEC, www.ecuadorencifras.gob.ec) over the Ecuadorian Amazon domain (0.5°N,77.5°W; 0°S,74.5°W; 5°S,79.5°W; 5°S,78.5°W), to finally average the precipitation and temperature values over this region from 1901 to 2019. Temperature and precipitation were defined as primary and secondary climate parameters for TRW and $\delta^{13}C_{TR}$, whereas for $\delta^{18}O_{TR}$ it was carried out contrariwise. September was specified as the ending month of tree growth, and the four season-lengths were set at 1, 6, 9, and 12.

2.5.2. Tree-ring isotope records and statistical relationships

We computed Pearson's correlation coefficients (r) between the $\delta^{18}O_{TR}$ and $\delta^{13}C_{TR}$ with the corresponding local and regional climate variables to quantify the statistical relationship. The local precipitation and temperature were averaged from Puyo (1965–2018) and Shell (1981–2018) instrumental stations and constituted the PAS local record. The cloud cover time-series was acquired from the CRU TS4.04 from 1930 to 2018 (Harris et al., 2020) for the Mera site (1°24′S, 78°03′W). In addition, the monthly mean Highly Reflective Cloud (HRC) product from the NOOA-ESRL Physical Sciences Laboratory was used. This dataset (1971–1985, 1° x 1° resolution) is a proxy for deep convection, indicating cloud systems responsible for most tropical rainfall deliberately excluding non-convective cold clouds (Garcia, 1985). It is available at https://psl.noaa.gov/data/dsets/hrc/. In the case of monthly temperature anomalies for Ecuador, these corresponded to the Berkeley Earth Land/Ocean Temperature Record and spanned from 1901 to 2018 (Rohde and Hausfather, 2020). Daily datasets (1980–2018) for insolation, sunshine duration, and low cloud cover were acquired from the National Aeronautics and Space Administration website (https://data.giss.nasa.gov/modelE/ar5plots/srlocat.html) and ERA-Interim reanalysis at 0.75° x 0.75° grid resolution (Dee et al., 2011). All calculations were run using the R statistical programming environment (R Core Team, 2020). On the other hand, spatial correlations were conducted using the KNMI explorer (Trouet and Van Oldenborgh, 2013). Records of Outgoing Longwave Radiation (OLR), successfully used as a proxy for deep convection in Tropical South America in previous studies (Hastenrath, 1997), were obtained from NCEP/NCAR Global Reanalysis Products at 2.5° x 2.5° resolution for the 1948–2018 period (NOAA, 1994). Cross wavelet coherence analysis was carried out using the open-source MATLAB package from Grinsted et al. (2004). The regional information for the demarcation of the SAMS borders was obtained from the IPCC WGI Interactive Atlas website (https://interactive-atlas.ipcc.ch) (Douville et al., 2021). Finally, backward HYSPLIT (HYbrid Single Particle Lagrangian Integrated Trajectory) air mass trajectories were calculated using the "PySPLIT" python package (Warner, 2018).

3. Results

3.1. Dendrochronology

3.1.1. Annual ring periodicity

The wood anatomical analysis in *C. nebulosa* showed a well-defined demarcation of rings due to the presence of a marginal band of parenchyma indicating the onset of the growing season (Fig. 2a). The vessels were arranged in radial and diagonal patterns with a diameter ≤ 350 μm and density ≤ 5 vessels/mm^2. In addition, larger vessels were clustered at the beginning of a new growing season (earlywood) in the parenchyma band with the presence of common tylosis and gums (Fig. 2b and c). Moreover, the annual formation of rings in *C. nebulosa* was successfully validated using radiocarbon (^{14}C) taking advantage of the post-1955 CE 'bomb-pulse', and the best fit was to the Southern Hemisphere Zone 3 (SHZ3) calibration curve (Hua et al., 2013) (Fig. 2d and Supplementary Dataset).

3.1.2. Tree-ring chronologies

The *C. nebulosa* trees showed an initial slow growth with a subsequent increase at intermediate years to finally stabilize at maturity, forming a sigmoidal-type growth curve (Supplementary Fig. S2). The first century of growth (1860–1960) did not vary considerably, and it is only from 1960 onwards that higher peaks are observed. Tree-rings were dated between the period 1860–2019. Most of the sampled trees were relatively young, with a mean of 46 years and an average ring-width of

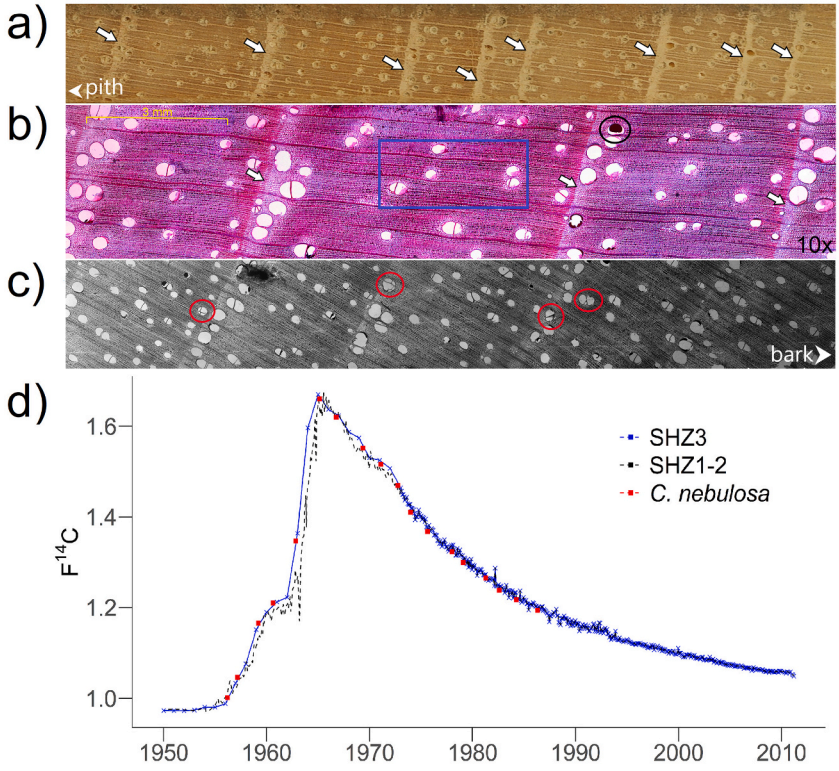

Fig. 2. (a) Wood cross-section of *C. nebulosa* showing the limits of growth rings defined by a thin band of marginal parenchyma (white arrows). (b) Microscopic structure of growth rings with the presence of gums in a vessel (black circle). Wide vessels are embedded in marginal parenchyma (white arrows), whereas wood formed later during cambial growth presents narrower vessels (blue rectangle). (c) Small to medium-sized vessels with the presence of tylosis (red circles). (d) Individual tree-rings measured by ^{14}C (red dots) over the bomb-spike for independent validation of ring annuity. The $F^{14}C$ calibration curves for Southern Hemisphere correspond to SHZ1–2 (in black) and SHZ3 (in blue) (Hua et al., 2013). (For interpretation of the references to colour in this figure legend, the reader is referred to the web version of this article.)

4.38 mm. The maximum age was found in a tree growing for 160 years from 1860 to 2019, whereas the minimum registered age was 31 years from 1989 to 2019. Tree stands presented an average diameter of 8.76 mm year^{-1}. The calculated EPS for the complete TRW chronology gave a value of 0.46 (1860–2019), increasing to 0.65 when considering a shorter period with higher sample replication (1960–2019) (Supplementary Dataset). Each averaged detrended individual allowed the construction of a mean standard chronology whose robustness increased after 1920 (Fig. 3a).

Regarding the tree-ring stable-isotope chronologies, interannual variation in the $\delta^{18}O_{TR}$ and $\delta^{13}C_{TR}$ records covered the period from 1864 to 2018 (154 years). The mean isotopic value for the composite $\delta^{18}O_{TR}$ chronology (Fig. 3b black curve) was 23.9 ± 1.2‰, with a minimum of 20.7‰ and a maximum of 26.8‰. In the case of $\delta^{13}C_{TR}$ record (Fig. 3c blue curve), the mean value was -27.7 ± 1.4‰ with values ranging from −29.9‰ (minimum) to -24.8‰ (maximum). Both $\delta^{18}O_{TR}$ and $\delta^{13}C_{TR}$ records revealed an upward trend towards more enriched isotopic values, although the $\delta^{13}C_{TR}$ indicated a long-term increase supported by a strong linear regression ($r = 0.83$). In the case of $\delta^{18}O_{TR}$, the rise seems to be moderate and more evident after the second half of the 20th century.

3.2. Dendroclimatology

3.2.1. Tree-ring width and seasonal climate signal

The seasonal correlations of temperature with TRW index were positive and significant ($p < 0.01$) from March to September in most of the evaluated season lengths at 1-, 6-, 9- and 12-months (Fig. 3a top). Calculations beyond September did not increase the correlations (not shown). By contrast, the end-of-the-year previous precipitation (Oct-Dec) found significant negative correlations in tree-ring development ($p < 0.05$), probably associated with the second precipitation maxima in the site (Fig. 1b). However, this trend is reverted from April until September, where a considerable reduction from negative to neutral correlation is visible (Fig. 4a bottom). These results suggest that radial growth is optimal under lower temperatures (Jun-Aug) and rainfall (Jun-Sep) in the area (Fig. 1).

On the other hand, the correlations between Ecuadorian Amazon temperature and precipitation climate parameters with $\delta^{18}O_{TR}$ and $\delta^{13}C_{TR}$, although large and positive, were not significant in most cases. The $\delta^{18}O_{TR}$ values present a low negative correlation with rainfall during all the evaluated 1-, 6-, 9- and 12-months showing a slight peak in the transition between austral summer to autumn (Feb-Mar) though not statistically significant (Fig. 4b top). On the other hand, a significant positive relationship ($p < 0.05$) with May-Aug temperatures (Fig. 4b bottom) was found, which are the months with the lowest values in the site according to Fig. 1c. Regarding the $\delta^{13}C_{TR}$ association with climate variables, precipitation has a neutral influence on the carbon chronology (Fig. 4c bottom). Conversely, the temperature was persistently correlated with the $\delta^{13}C_{TR}$ across the seasons, but these relationships were insignificant. Overall, these results indicate that local temperature and precipitation seem to be pivotal factors regulating TRW growth forest dynamics during austral winter (Jun-Sep). A clear seasonal climate signal could not be obtained for $\delta^{18}O_{TR}$ and precipitation, but a large continual positive influence of temperature for the cooler months (May-Aug) for $\delta^{18}O_{TR}$ and $\delta^{13}C_{TR}$ is remarkable.

3.2.2. Oxygen isotopes and western Amazon precipitation

Similar to the previous results employing $\delta^{18}O_{TR}$ and the averaged CRU from the Ecuadorian Amazon domain (Fig. 4b), the Pearson's correlation coefficient between $\delta^{18}O_{TR}$ chronology and local Mera (1°24′S, 78°03′W) CRU precipitation (1921–2018) during the wettest period March to June gave an $r = 0.07$ ($p < 0.05$). The correlation increased when employing the instrumental PAS precipitation (1965–2018), obtaining an $r = 0.24$ ($p < 0.05$). Presumably, the low correlations with local CRU precipitation obey to the small number of

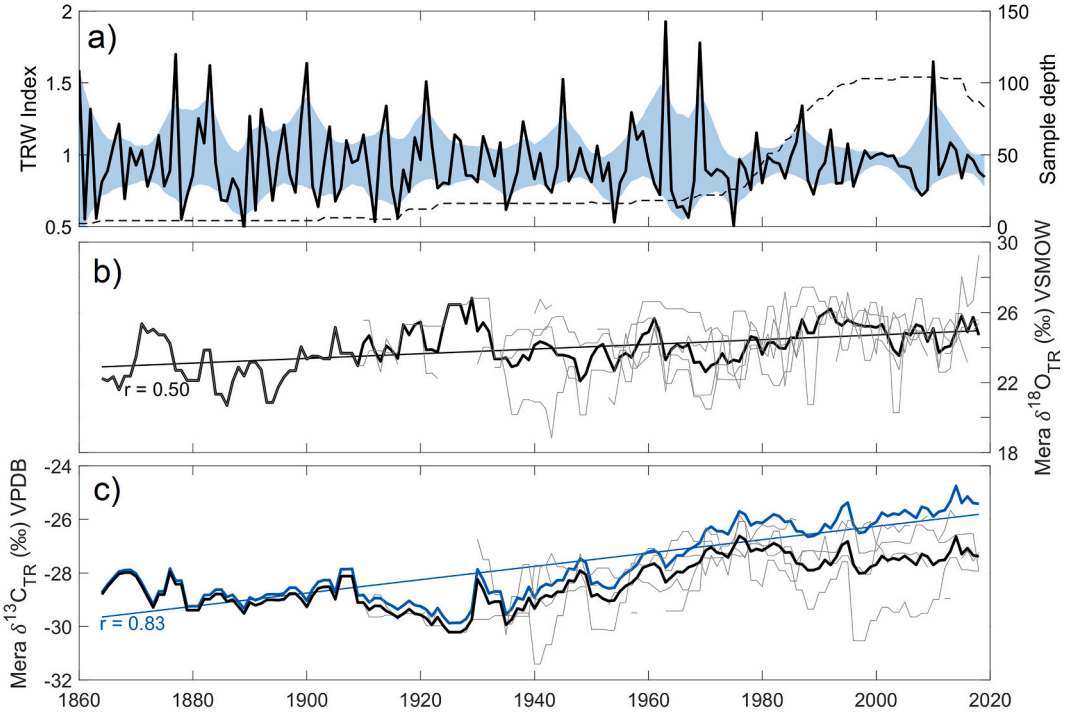

Fig. 3. Built tree-ring chronologies of *C. nebulosa* for Mera, Ecuador. (a) TRW standard chronology and 95% confidence intervals (CI) (blue stripe) obtained from 24 trees from 1860 to 2019. The superimposed dashed line corresponds to the number of individuals (sample depth) used for its construction. Tree-ring (b) $\delta^{18}O$ and (c) $\delta^{13}C$ values from single trees ($n = 4$, gray lines) with their mean composite chronologies (black curves) superimposed with an Ordinary Least Squares regression (black and blue lines) from 1864 to 2018. The other blue chronology in (c) corresponds to the corrected $\delta^{13}C_{TR}$ composite chronology (black curve) relative to pre-industrial standard values, according to McCarroll and Loader (2004). (For interpretation of the references to colour in this figure legend, the reader is referred to the web version of this article.)

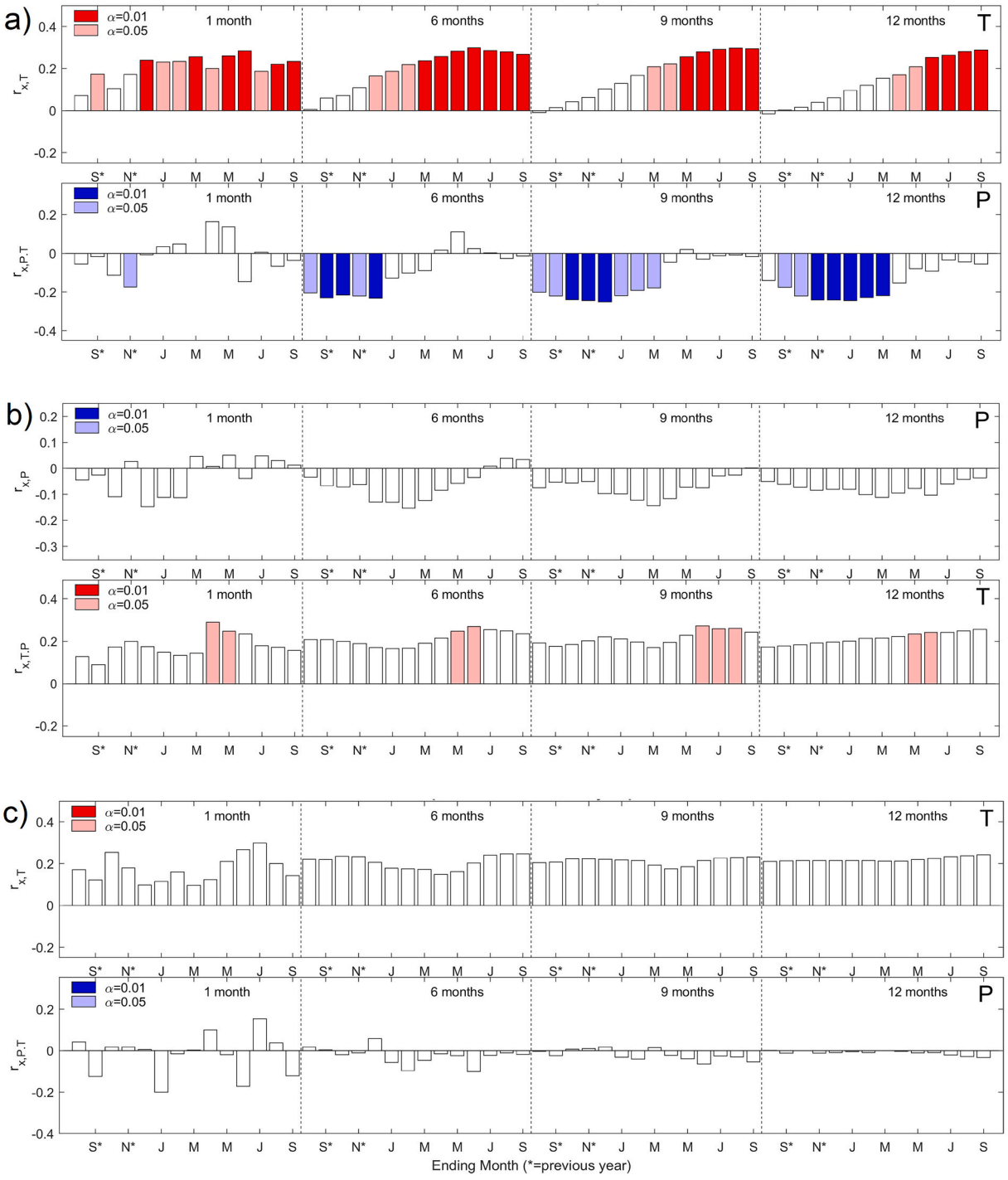

Fig. 4. Simple and partial correlations of the constructed Mera tree-ring series (TRW, $\delta^{18}O_{TR,}$ and $\delta^{13}C_{TR}$; $p < 0.05$) with seasonalized CRU climate variables (temperature and precipitation) over the Ecuadorian Amazon from 1901 to 2019 (a) Partial correlation between TRW with primary temperature (top) and precipitation (bottom) (b) Partial correlation between $\delta^{18}O_{TR}$ with primary precipitation (top) and temperature (bottom) (c) Partial correlation between $\delta^{13}C_{TR}$ with primary temperature (top) and rainfall (bottom). Notation r_x, T at the ordinate axis means, e.g. correlation of x (TRW) with T (temperature); r_x, PT means partial correlation of x with P (precipitation), controlling for the influence of T.

stations that conformed the gridded data at this latitude. Therefore, a spatial analysis at a regional scale in the same humid months (Mar-Jun) between $\delta^{18}O_{TR}$ and the CRU rainfall product significantly improved the correlations to $r = -0.50$ (1921–2018, $p < 0.01$) in the northwestern area of the Amazon Basin (Fig. 5a). Interestingly, this spatial correlation is also present at this latitude when using $\delta^{18}O_{TR,}$ and Outgoing Longwave Radiation (OLR in W m^{-2}) derived from NCEP-NCAR reanalysis, although evaluated for a shorter period (1985–2018, $p < 0.05$, Fig. 5b). Taken together, these results suggest that there is an association between $\delta^{18}O_{TR}$ from the Mera site and a strong convective area in the Amazon basin moving northwards, which dynamics have been previously described by Hastenrath (1997) (Supplementary Fig. S3).

A frequency analysis between CRU precipitation over the detected convective area and the $\delta^{18}O_{TR}$ (Fig. 5c top) shows a significant coherence in most of the records, especially from 1920 to mid-1970 ($\alpha < 0.05$), indicating a periodicity between 4 and 8 years. In contrast,

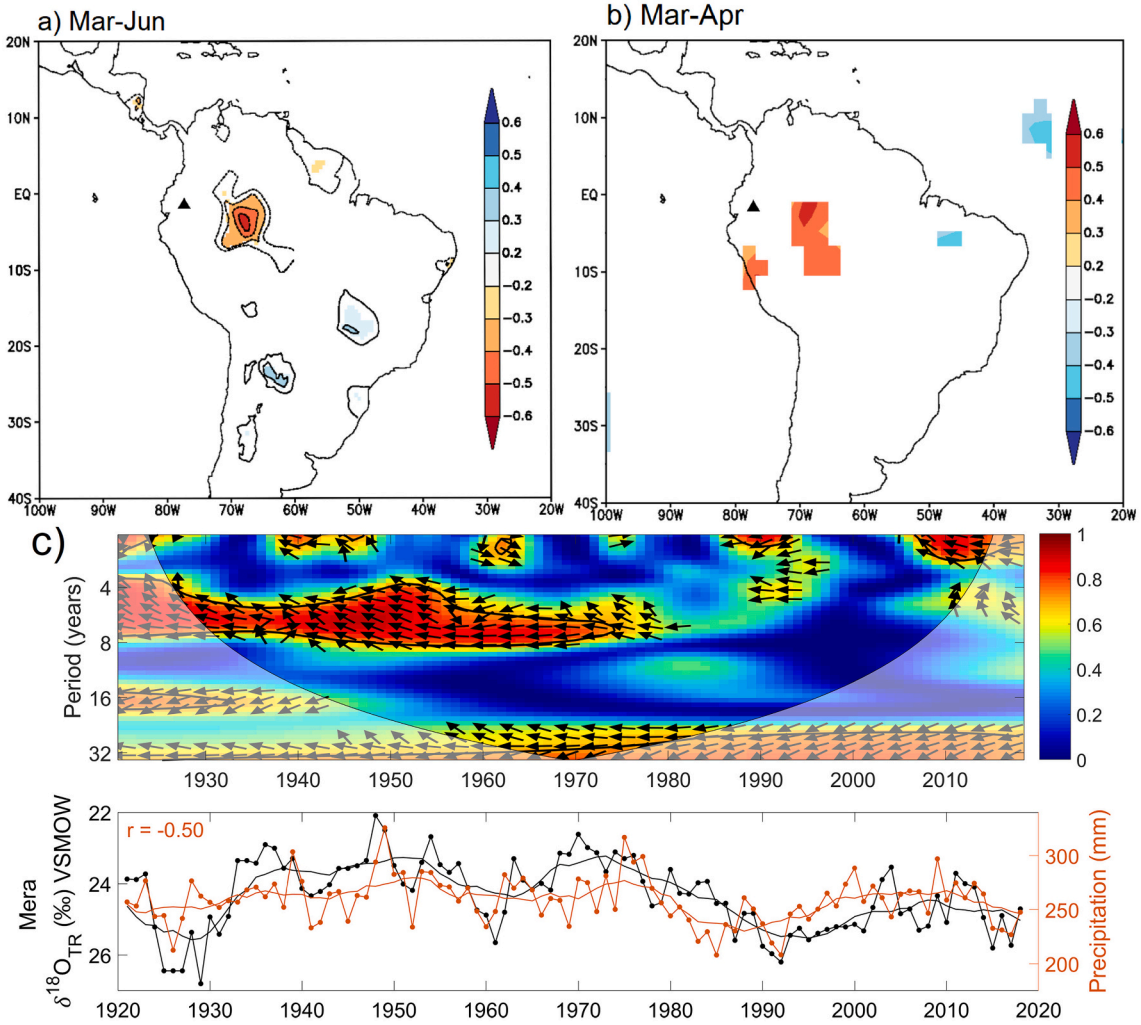

Fig. 5. (a) Spatial correlation fields between Mera $\delta^{18}O_{TR}$ with wetter March–June CRU precipitation (1921–2018). The colour bar indicates the strength of the correlation coefficients significant at $p < 0.01$. (b) Spatial correlation between Mera $\delta^{18}O_{TR}$ with March–April Outgoing Longwave Radiation (OLR, 1985–2018) significant at $p < 0.05$ and derived from NCEP-NCAR reanalysis. OLR aids in locating areas of deep tropical convection and is a proxy for precipitation. In all graphs, the location of the Mera site is indicated by a black triangle. (c) Wavelet coherence (top) with its respective time-series (bottom) between Mera $\delta^{18}O_{TR}$ and western Amazon precipitation from CRU (1921–2018) averaged over the orange-red zone in (a). Red areas bordered by black contour lines indicate significant coherence ($\alpha < 0.05$), whereas arrows pointing left indicate anti-phase angle. The shading indicates areas outside the cone of influence. Each record is superimposed with a 10-year Moving Average for the time-series, and the correlation is significant at $p < 0.05$. In the case of the Mera $\delta^{18}O_{TR}$, the scale is reversed (black curve). (For interpretation of the references to colour in this figure legend, the reader is referred to the web version of this article.)

associations are not significant from 1980 onwards, although significant regions displaying anti-phase angle (arrows pointing left) are consistent in most of the analysis. Similarly, the time-series in Fig. 5c (bottom) have an analogous interdecadal variation which even captures the apparent drop in precipitation at the end of 1970, followed by an increase at the beginning of 1990, which suggests a common regional control in their moisture source. It is apparent from these results that $\delta^{18}O_{TR}$ does not correlate well with a local rainout, but it is regulated by Amazon basin-intrinsic processes in agreement with previous studies (Baker et al., 2016; Brienen et al., 2012; Villacís et al., 2008; Vimeux et al., 2005).

3.2.3. *Carbon isotopes and temperature controls*

The carbon isotopes for the Mera site showed a significant correlation ($r = 0.51$, $p < 0.05$) with CRU cloud cover (1930–2018) (Fig. 6). Similarly, the $\delta^{13}C_{TR}$ correlations with instrumental PAS temperature (1965–2018) gave a value of $r = 0.53$ ($p < 0.05$) and an even higher correlation $r = 0.67$ ($p < 0.05$) was obtained with the temperature anomalies for Ecuador (1901–2018). The evaluated period was July–August in all cases, which corresponded to the lower temperature season (Fig. 1c). There is a consistent upward trend between $\delta^{13}C_{TR}$ with all the assessed climatic factors. In contrast, correlations with PAS relative humidity gave a negative correlation of −0.53 ($p < 0.05$) (not shown). To shed further light on their seasonality, time-latitude diagrams of cloud cover, temperature, relative humidity, and soil moisture averaged over the longitudes 80°W-75°W (Ecuadorian Amazon) are presented in Supplementary Fig. S4. This set of graphs shows that their values over the year are broadly coherent in this region, exhibiting the lowest values from June to September (less-wet months) and indicating their synchronous temporal variability.

4. Discussion

4.1. *Cedrela nebulosa growth*

Studies on dendroclimatology in Ecuador are scarce. The available literature has focused on dry forests and their possible teleconnections with ENSO, especially in the south of the country (Pucha-Cofrep et al.,

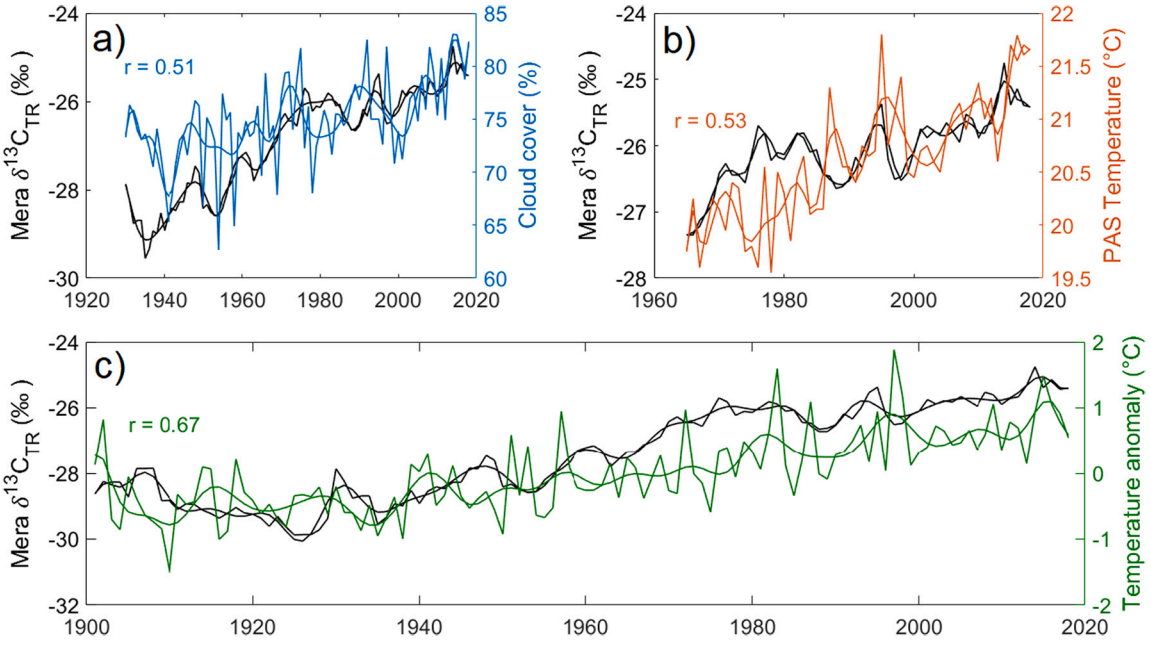

Fig. 6. Carbon isotopes $\delta^{13}C_{TR}$ (black curve) correlated with (a) CRU cloud cover (1930–2018), (b) Puyo and Shell (PAS) temperature (1965–2018), and (c) Temperature anomalies (1901–2018) relative to the period of January 1951–December 1980 average for Ecuador from the Berkeley Land/Ocean Temperature Record (http://berkeleyearth.org/data/). In all the graphs, the analyzed interval corresponds to July–August. A cubic spline was superimposed to each time-series to visualize long-term variability.

2015). Previous studies employing the genus *Cedrela* have been carried out mainly with *C. odorata* (Nacimba, 2015) and *C. montana* (Baker, 2017; Volland et al., 2015). For *C. nebulosa,* this study is the first investigation that addresses its dendroclimatic potential in Ecuador in a pre-montane forest and the second in South America. Prior research using *C. nebulosa* was recently conducted in the montane Andean forest of Peru in the Junin Department (Layme-Huaman et al., 2018) and served as a reference to compare some of our findings. The Mera TRW chronology (1860–2019) shows a low EPS of 0.46 due to the small sample replication of individuals before 1920 (Supplementary Dataset). The period from 1960 to 2019 covers the largest number of trees (Fig. 3a) and provides a significant increment in EPS to 0.65, but still lower when compared to the *C. nebulosa* in the Peruvian Andes, which gave an EPS of 0.91 (23 series-13 trees) (Layme-Huaman et al., 2018). A similar situation of a less than 0.85 EPS threshold was recently encountered in another newly constructed chronology from a tropical montane forest in Cajas National Park, Ecuador using *Polylepis reticulata.* EPS values above 0.85 in the chronologies (1821–2015) were reached only after 1990 (Alvites et al., 2019), suggesting that ~14% of the constructed chronology satisfied the established 0.85 cut-off. Hence, this only illustrates that low EPS values can be expected principally due to the lack of long-lived individuals when employing a new species in tropical dendrochronology. In our case, despite field exploration efforts (Supplementary Fig. S1), only a few long-lived *C. nebulosa* trees were found, which overall has contributed to a low sample replication and a subsequent low EPS in the final TRW chronology (Fig. 3a).

In general, the EPS estimates the variance fraction of an infinite hypothetical population expressed by the chronology, and a general 0.85 in EPS is considered a robust chronology for climate studies (Wigley et al., 1984). Nevertheless, there is an ongoing debate about the application of EPS to evaluate the suitability of tree-ring data for climate reconstruction purposes. In fact, the assigned 0.85 threshold originally appeared as an example for another statistical parameter used in dendrochronological studies (Subsample Signal Strength) and is advised not to be taken as a rule for accepting or rejecting chronologies (Buras, 2017; Wigley et al., 1984). Although it might affect the local strength of the obtained correlations between TRW and local climate parameters, this shortcoming affected neither the results nor the main conclusions of this study, mainly based on the use of oxygen and carbon stable isotopes. However, this does not mean that the dendrochronological part was undertaken lightly. On the contrary, a proper tree-ring delimitation and cross-dating were successfully achieved by two independent and complementary tools, wood anatomy and radiocarbon (Fig. 2), accomplishing this initial task before undertaking subsequent isotopic analysis in the tree-rings (van der Sleen et al., 2017). Annual validation of growth rings in tropical trees is not always straightforward. Despite the extensive evidence of annual ring formation in *Cedrela*, there is an indication that this genus may form more than one ring per year, especially in aseasonal climates (Baker et al., 2017). Hence, independent confirmation of the annual periodicity at a new site is always advisable at tropical latitudes, as was carried out in this paper (Supplementary Dataset).

The calculated monthly correlations showed that *C. nebulosa* TRW is primarily controlled by seasonal temperature fluctuations regarding the growing season. It goes from February–March to September, encompassing the wettest (Apr-Jun) and less-wet (Jul-Sep) months at this latitude (Fig. 4). These results match those observed in early studies in *Cedrela* in Central Amazon, which indicates that cambial growth is determined by the change from wet to dry season (Dünisch et al., 2002). In addition, this study supports evidence from previous observations in Ecuador using *C. montana* and *C. odorata* (Bendix et al., 2006a; Nacimba, 2015), which found similar tree phenologies. These studies showed that *Cedrela* trees were leafless from October to December (austral spring-summer), flowering from January to April (austral summer-autumn), and fruiting from May/June to September (austral winter-spring) (Supplementary Fig. S1). Hence, the phenology of *C. nebulosa* is closely related to *C. montana* and *C. odorata,* as thoroughly described by Koecke et al. (2013), being endemic to the Andes.

Comparing our findings with those of Bräuning et al. (2009) using *C. montana* from southern Ecuador confirms the link between TRW and temperature in *Cedrela*, although the growth period was from January to April. Contrasted with its counterpart from the Peruvian forest, our results are also in agreement with the conclusion that temperature is the primary controller of annual ring growth (Layme-Huaman et al., 2018). However, in our study, ENSO did not significantly influence local

temperature variations, contrary to the close association found with the Multivariate ENSO index and Pacific Ocean SST reported for *C. nebulosa* from Peru. In Ecuador, ENSO affects regions near the Pacific coast and southwest of the Andes mountain range (Vuille et al., 2000). Its effect is unclear for the Ecuadorian Andean eastern slope and Amazon region where the Mera site is located (Ilbay-Yupa et al., 2021; Vuille et al., 2000). Therefore, the observed temperature variations in our study region could be attributed to the insolation variability over the course of the year, which presents a bimodal peak during March and September equinoxes along with a lower amount of solar radiation during June solstice, which is likely accountable for the ~2 °C decrease in temperature shown in Fig. 1c. Overall, these results further support that temperature is the major factor controlling TRW in *C. nebulosa* at western Amazon.

4.2. Tree-ring oxygen isotopes and western Amazonian precipitation

The Mera $\delta^{18}O_{TR}$ record was not significantly correlated with local precipitation values. However, it gave better results with upstream precipitation from the western Amazon basin, capturing most of the interdecadal variability during the primary wet season (Mar–Jun) and showing an anticorrelation between $\delta^{18}O_{TR}$ with the rainfall in the zone (Fig. 5). The SAMS climatological onset and demise correspond to the end of October until March, respectively, exhibiting its mature phase during December–February (Raia and Cavalcanti, 2008; Vuille et al., 2012). When the intra-annual rainfall variability shifts from austral summer (Dec-Feb) towards northernmost latitudes reaching Ecuador (5° S-1° N), the SAMS has already attained its demise phase (Mar-May). Hence, the primary system controlling the precipitation variability is the ITCZ (Fig. 7). The spatial correlation ($r = -0.50$) obtained between the Mera $\delta^{18}O_{TR}$ with wetter March–June CRU precipitation (1921–2018; Fig. 5) reflects the monsoon withdrawal and a clear ITCZ signal (Garreaud et al., 2009; Raia and Cavalcanti, 2008; Vuille et al., 2012).

In addition, Supplementary Fig. S3 shows the monthly mean OLR climatology during the year. The low OLR values (<240 W m^{-2}) correspond to cold and high clouds that denote enhanced convection, represent the regional position of the ITCZ and the associated location of rainfall (Hastenrath, 1997; Poveda et al., 2006; Villacís et al., 2008). Values between 200 and 220 W m^{-2} are mainly observed within the Amazon Basin and overlap the previous spatial correlation between $\delta^{18}O_{TR}$ and CRU rainfall presented in Fig. 5. The region (5°S-0°N, 71°W-65°W) observed in Figs. 5a most likely corresponds to a highly convective area probably associated with the recently described equatorially symmetric mode (see Fig. 1 in Garcia and Kayano, 2010). This mode represents convection occurring during the transition seasons from dry to wet and vice-versa in the western equatorial Amazon and does not represent the monsoon character of the convection over the Amazon (Garcia and Kayano, 2010).

Furthermore, the robust relationship between the $\delta^{18}O_{TR}$ and regional precipitation is consistent with previous observations

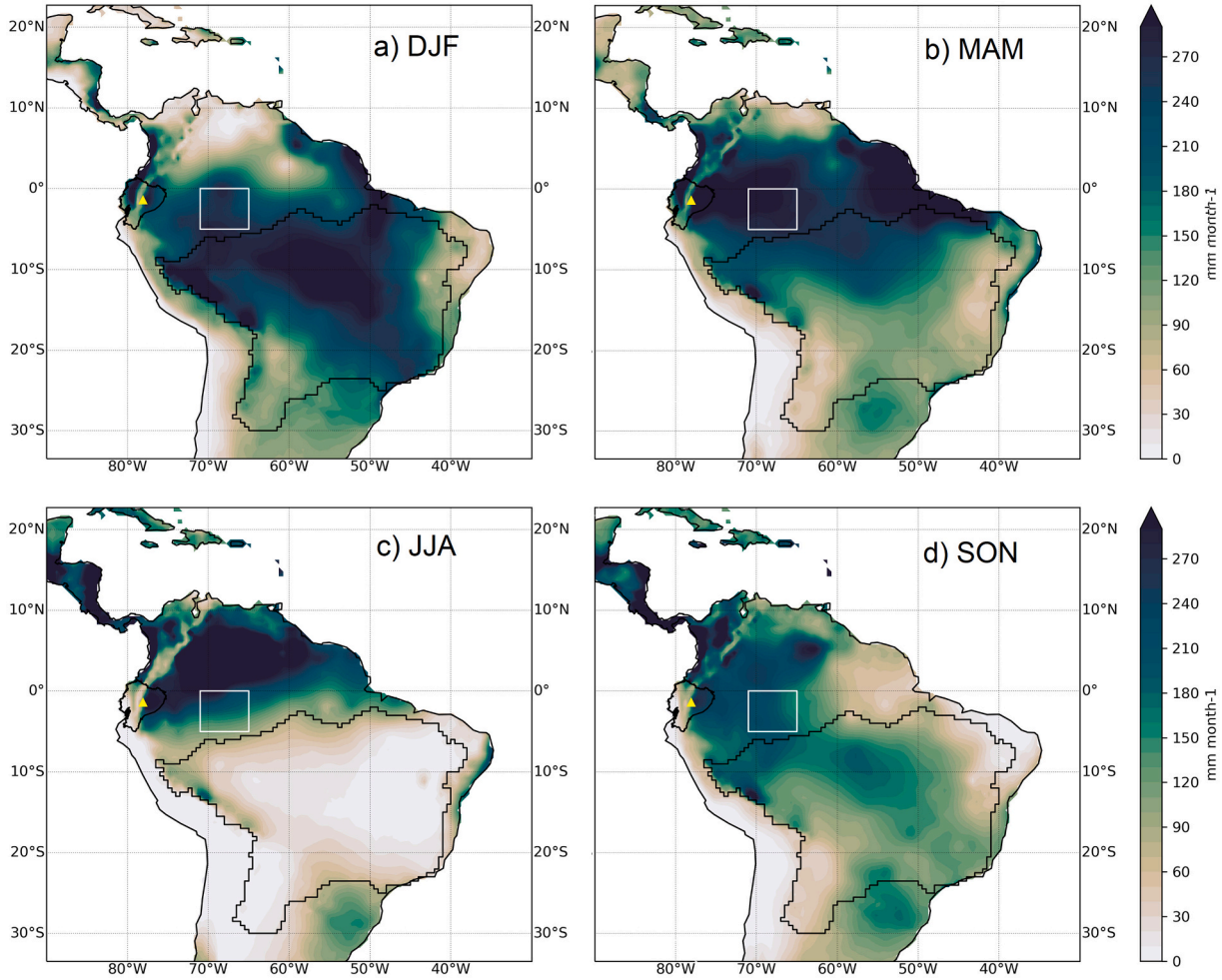

Fig. 7. Annual seasonal precipitation in South America during (a) Dec-Feb (b) Mar-May (c) Jun-Aug and (d) Sep-Nov. The area of influence of the SAMS and the Ecuadorian territory borders are indicated. The yellow triangle in all insets marks the Mera study site, whereas the correlated convective region (5° S-0° N, 71° W – 65° W) with $\delta^{18}O_{TR}$ is shown in the white rectangle. The precipitation values correspond to the CRU dataset (1901–2019) and are expressed in mm $month^{-1}$. (For interpretation of the references to colour in this figure legend, the reader is referred to the web version of this article.)

indicating that rainout upstream in convective areas better explains the seasonal variations in $\delta^{18}O_{prec}$ (Villacís et al., 2008; Vimeux et al., 2005). This isotope-climate relationship is characteristic of tropical precipitation, which is highly convective at low latitudes (Hastenrath, 1997; Kurita et al., 2009). Another important finding is the marked period of 4 and 8 years in the wavelet coherence analysis between the $\delta^{18}O_{TR}$ and western Amazon rainfall records (Fig. 5c). These results are most likely related to variations in Sea Surface Temperature (SST) in the Tropical North Atlantic, which is the primary moisture source to the continent and is responsible for the seasonal displacement of the ITCZ (Baker, 2017; Yoon and Zeng, 2010) (Supplementary Fig. S6). Although ENSO has a similar periodicity (2–7) years, a recent regionalization of precipitation in Ecuador showed a minor influence on our site (Ilbay-Yupa et al., 2021). Overall, this evidence supports the potential use of *C. nebulosa* as a proxy for the western Amazon wettest season (Mar-Jun) responding to a convective regional hydroclimate process regulated by the ITCZ. This finding broadly supports other studies linking $\delta^{18}O_{TR}$ variability to intrinsic processes within the Amazon basin (Baker et al., 2016; Brienen et al., 2012). A note of caution is due here since other plant physiological effects may alter the isotopic signal of precipitation before its final fixation in the wood (i.e., leaf water enrichment) (Treydte et al., 2014). Nevertheless, our findings suggest that the $\delta^{18}O_{TR}$ variability is chiefly determined by those of meteoric rainwater. Previous studies on *Cedrela odorata* in Bolivia have shown that this genus has a superficial root-system and water is uptake from the topsoil layer (Brienen et al., 2012). Furthermore, the leaf water enrichment effect is low as atmospheric humidity is high during most of the year in the Mera site (86% average: 1965–2018), reducing transpiration rate (Supplementary Fig. S4c). Finally, a comparison between our *C. nebulosa* $\delta^{18}O_{TR}$ record with *C. montana* from Cuyuja-Ecuador (see location in Fig. 1a) (Baker et al., 2018) for the common period of 1864–2012 found a correlation of $r = 0.35$ ($p < 0.05$) (Supplementary S5). A synchronic periodicity between 4 and 10 years is observable and likely reflects their joint response to SST oscillations in the Tropical North Atlantic. Most of the Ecuadorian Amazon moisture paths calculated by HYSPLIT back trajectories come from the Atlantic Ocean (Supplementary Fig. S6), with a minor contribution from the Pacific domain during the year except in austral summer (Dec-Feb), when air parcels 6 km above ground level are frequent. In addition, air parcels during the more humid March–June months present a clear eastern provenance, giving a robust integrated signal at this time of the year over the Amazon basin. There are noticeable differences at an interannual scale in the records due to sampling replication (resolution), forest type, altitude, and latitude effect, but overall, they show a coherent variability and become more alike when observed at decadal scales. In general, our findings are in agreement with those obtained by Brienen et al. (2012) indicating that tree-rings preserve the signal of oxygen isotopes during the wet season, with weaker influence of temperature. In addition, the authors found that the water-vapor transport processes along the pathway to the site is the key factor controlling the meteoric isotopic signal ultimately incorporated into the tree structure. Therefore, the low-level jets such as Orinoco (950–800 hPa, Dec-Feb) and the Equatorial mid-tropospheric easterly jet (700 hPa, Mar-Aug) (Jiménez-Sánchez et al., 2020; Poveda et al., 2014) seem to be the wind corridors carrying atmospheric moisture towards Ecuador (Supplementary Fig. S6). Eventually, they could be the link between the ITCZ and SAMS systems by feeding the South American low-level jet. This may provide evidence for the observed strong correlation of $\delta^{18}O_{TR}$ from the northwest to the southwest Amazon hydrology (Brienen et al., 2012), being an important issue for further research.

4.3. Tree-ring carbon isotopes and role of cloud cover

The high positive correlations obtained with local temperature ($r = 0.53$), temperature anomalies ($r = 0.67$), and cloud cover ($r = 0.51$) suggest that photosynthetic rate A is the primary control in the $\delta^{13}C_{TR}$ record, and cloudiness is a crucial factor in this climate system. During the season of lower precipitation from July to September (Fig. 1b and Fig. 7), cloud cover has a significantly reduced percentage compared to the other seasons (Fig. 8a). Its seasonality is strongly associated with the movement of the ITCZ, and therefore mirrors the reduction in rainfall during this period. In fact, Bendix et al. (2006b) found that the seasonal cycle of cloudiness was significantly correlated with the spatial occurrence of the rainy seasons in Ecuador. Cloud cover and sunshine duration are strongly anticorrelated ($r = -0.89$, Fig. 8b). Lower cloudiness reduces albedo but increases sunshine duration, enhancing the photosynthetic rate during the less-wet season from July to September. Higher cloud fraction in the wet season absorbs Photosynthetically Active Radiation (PAR), affecting photosynthesis and flowering (Bendix et al., 2008; Günter et al., 2008). In fact, flowering and fruit production are synchronized with drought periods and sunny conditions and are indicators of reduced cloud cover percentage. Therefore, this may also be the case for *C. nebulosa* trees. Prior studies on *Cedrela* and field observations confirm that fruiting starts during the season of lower precipitation (Aug-Sep) (Nacimba, 2015; Pennington and Muellner, 2010), where sunshine duration contrasts to low cloud cover (Fig. 8b). Several reports have shown that *C. montana*, which shares part of *C. nebulosa* geographical range and occupies a similar ecological niche (Pennington and Muellner, 2010), can be considered a light-demanding species (Bräuning et al., 2008). As previously discussed in Section 4.1 regarding the common temperature influence on cambial growth for *C. montana* and *C. nebulosa,* probably such connection with light availability may also be present; hence this species must also be light-demanding. Ultimately, our observations are in accord with those suggesting that highly reflective clouds (HRC), a measure of deep organized tropical convection, must characterize the region between 10°N to 10°S linked with the ITCZ's movement (Fig. 8a) (Garcia, 1985; Managave and Ramesh, 2012). It can therefore be assumed that July to September are the months with a significant decrease in convective activity (Cumulonimbus cloud cluster) owing to the northernmost position of the ITCZ in these months (Hastenrath, 1997).

Regarding the stomal conductance g, the annual temporal variability of relative humidity and soil moisture indicates that both are chiefly driven by precipitation. Their interannual variability shows lower values during the less-humid months of July–September, with an increment during April–June and October–November, matching what is observed in the rainfall pattern modulated by the ITCZ (Supplementary Fig. S4c and d). The reduction in the amount of rainfall at the end of the wet peak (Apr-Jun) is likely to diminish the water availability and, therefore, air humidity and soil moisture. Although relative humidity is inversely proportional to temperature, the ~2 °C drop (Jun-Aug) is a minimum value to significantly raise the percentage of relative humidity to average (e.g., Jan–May). Overall, the decline in rainfall can account for an almost 2% decrease in relative humidity compared to the more humid season. Similar to relative humidity, precipitation was not significantly correlated with $\delta^{13}C_{TR}$.

These findings show that lower precipitations in July–September enhance the rate of photosynthesis, where the photosynthetic rate (A) (increasing temperature, higher photon flux/low cloud cover) outweighs stomatal conductance (g) (lower relative humidity and soil moisture lead by precipitation) (Fig. 8b). This results in a decrease in the internal concentration of CO_2 (c_i) and a more significant proportion of atmospheric $^{13}CO_2$ (during CO_2 assimilation) moving through the pathway as carbohydrates, then being transported to the cambium to be finally incorporated into the wood (Gagen et al., 2011; van der Sleen et al., 2017). Therefore, we interpret the $\delta^{13}C_{TR}$ as a rise in photosynthetic rate during the less-wet season (Jul–Sep) characterized by higher sunshine duration (>300 h month^{-1}/10 h day^{-}1), regulated by cloud amount and ultimately driven by ITCZ excursions (Fig. 8). Admittedly, in November, the ITCZ dynamics involve another second rainfall maxima, but it has a lower intensity. We assume that this does not significantly influence the $\delta^{13}C_{TR}$ because this peak does not occur during the

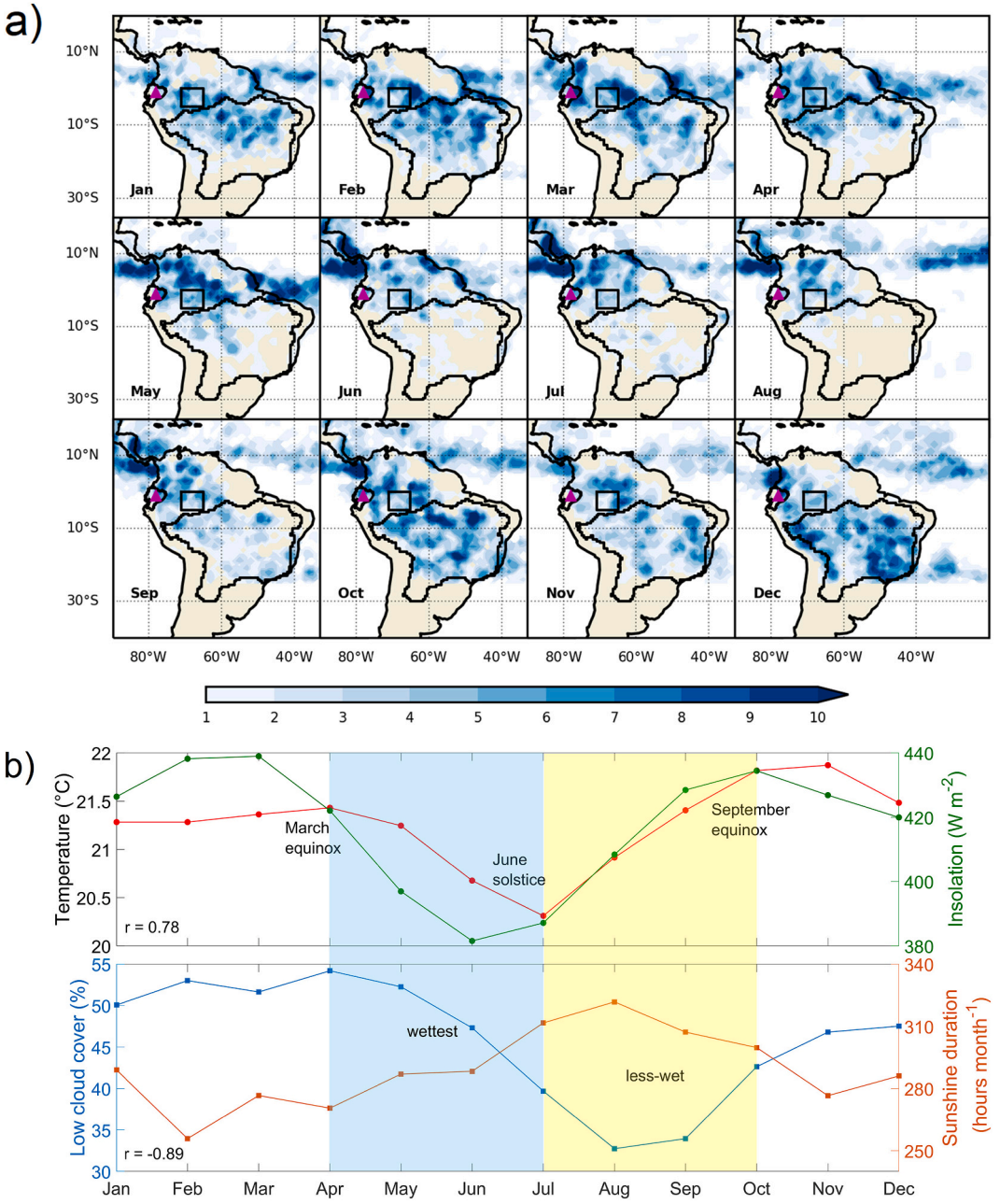

Fig. 8. (a) Monthly mean Highly reflective cloud from NOOA-ESRL Physical Sciences Laboratory (1971–1985) over South America expressed as the average number of days with HRC per month. The area of influence of the SAMS and the Ecuadorian territory borders are indicated. The previously identified convective region is also shown in the black rectangle. The Mera study site is marked with a magenta triangle. (b) Seasonal patterns of the principal climate variables associated with changes in temperature in the Mera site. (Top) PAS temperature (1965–2018) and monthly insolation (1980–2018) from the National Aeronautics and Space Administration (https://data.giss.nasa.gov/modelE/ar5plots/srlocat.html). Equinoxes happen on the 22 of March and 22 of September approximately. Conversely, the solstice occurs around June 20th. (Bottom) Low cloud cover (from surface to 2 km) and sunshine duration were obtained from the ERA-Interim for 1980–2018. On average, the sunshine duration is 274 h month^{-1}/9 h 7 min day^{-1} (Jan-Mar), 282 h month^{-1}/9 h 24 min day^{-1} (Apr-Jun), 314 h month^{-1}/10 h 27 min day^{-1} (Jul-Sep), and 287 h month^{-1}/9 h 34 min day^{-1} (Oct-Dec). Pearson's correlation coefficient between the variables in each inset is shown at the bottom left at $p < 0.05$. (For interpretation of the references to colour in this figure legend, the reader is referred to the web version of this article.)

growing season of March–September (see Section 3.2.1) but during the dormancy period in November–December. Although we potentially have a signal for the entire year in tropical trees because growth does not necessarily cease (Gagen et al., 2011), the synchronous shifts in the meteorological parameters are especially predominant and stronger during July–September (Supplementary Fig. S4), and *C. nebulosa* trees are actively synchronized with them.

5. Conclusions

The purpose of the study was to elucidate the primary rainfall system controlling the Ecuadorian eastern Amazon precipitation between the SAMS and the ITCZ. For this purpose, oxygen ($\delta^{18}O_{TR}$) and carbon ($\delta^{13}C_{TR}$) chronologies were constructed using *Cedrela nebulosa* tree species in the Mera site, central Ecuador.

Preliminary dendrochronological work permitted the construction of an annual TRW record from 1860 to 2019 (160 years). The annuity of

rings was visually identified by wood anatomy and independently confirmed with radiocarbon (^{14}C) using the "bomb-pulse" (1955–2000). We also established the $\delta^{18}O_{TR}$ and $\delta^{13}C_{TR}$ records from 1864 to 2018, which are to date the firsts for this species near the South American equator.

Regarding climate-growth relationships, partial correlations showed that *C. nebulosa* TRW is primarily controlled by seasonal temperature fluctuations. The growing season at this latitude goes from March to September, covering the wettest (Apr-Jun) and less-warm (Jul-Sep) months. Similar significant seasonal climate signals could not be obtained for $\delta^{18}O_{TR}$ and $\delta^{13}C_{TR}$, but a large continual positive influence of temperature was observed mainly for the cooler months (May-Aug).

Spatial correlations between our $\delta^{18}O_{TR}$ record with regional western Amazonian rainfall revealed significant correlations ($r = -0.50$) and coherent anti-phase relationship (4−8 years) during March to June (wettest season). The synchronous pattern was mainly observed at decadal time scales. We concluded that the consistent long-term trend displayed in both records primarily reflects the ITCZ passage during the most humid months (Mar-Jun) and does not account for any monsoonal influence, which has withdrawn at this period of the year. Similar results obtained in an interdecadal comparison with a *C. montana* $\delta^{18}O_{TR}$ record from the same region (positive in correlation and in-phase coherence) overall support that *C. nebulosa* $\delta^{18}O_{TR}$ records the western Amazon precipitation isotopic signal during the wettest season.

The second significant finding was the identification of cloud cover as a vital controller of sunshine duration, which influences the phenology of *Cedrela nebulosa*. Indeed, we showed that cloud cover reduction during July–September increases the sunshine duration (>10 h day^{-1}) for *Cedrela nebulosa,* which is likely to be a light-demanding species. Therefore, the $\delta^{13}C_{TR}$ record is interpreted to reflect variations in the photosynthetic rate during light-increased and less-humid months (Jul-Sep) regulated by the passage of the ITCZ.

A limitation of this study is that the EPS was below the standard 0.85 thresholds commonly reported in dendrochronological studies for TRW, but the climate signal remained strong. In humid tropical forests, as in the case of the Mera site, the tree stands have continuous water input and a steady temperature (Fig. 1). Therefore, the climatic signal reflected in the width of the rings is very slight. However, microsite conditions, e.g., cloud cover, soil type, nutrients, humidity, light availability, become the significant climatic factors for tree growth, mainly observed in the $\delta^{13}C_{TR}$ record in this study. Despite the relatively low number of trees ($n = 4$) for isotopic studies, *C. nebulosa* $\delta^{18}O_{TR}$ and $\delta^{13}C_{TR}$ results showed a strong climate signal owing to the intrinsic processes in the Amazon basin driven by the ITCZ excursions. This work offers valuable insights into our understanding of the seasonal extension of the SAMS domain and the influence of the ITCZ in tropical northwestern South America, especially observed during the months of monsoon withdrawal and the onset of the ITCZ. Even though the ITCZ and SAMS climatology and boundaries have been thoroughly modeled and established (e.g. Garcia and Kayano, 2010; Murakami and Nakazawa, 1985; Raia and Cavalcanti, 2008; Schneider et al., 2014; Vuille et al., 2012; Wang et al., 2013; Zhou and Lau, 1998), our contribution is the first dendroclimatological study in Ecuador and Northern South America to show the ITCZ imprint in a tree-ring archive. Thereby, the insights gained from this study may assist future calibration of paleoclimate records and revision of previously interpreted archives at this tropical latitude.

Declaration of Competing Interest

The authors declare that they have no known competing financial interests or personal relationships that could have appeared to influence the work reported in this paper.

Acknowledgments

The research was supported by the European Union and the State of Hungary, co-financed by the European Regional Development Fund in the project of GINOP-2.3.2-15-2016-00009 'ICER'.

Appendix A. Supplementary data

Supplementary data to this article can be found online at https://doi.org/10.1016/j.gloplacha.2022.103791.

References

Alvites, C., Battipaglia, G., Santopuoli, G., Hampel, H., Vázquez, R.F., Matteucci, G., Tognetti, R., 2019. Dendrochronological analysis and growth patterns of Polylepis reticulata (Rosaceae) in the Ecuadorian Andes. IAWA J. 40, 331–S5. https://doi.org/10.1163/22941932-40190240.

Baker, J.C.A., 2017. Unravelling the Drivers of Short- and Long-Term Variability in the Amazon Hydrological Cycle Using Tree-Ring Oxygen Isotopes. Unravelling Drivers Short-and Long-Term Var. Amaz. Hydrol. Cycle Using Tree-Ring Oxyg. Isot. The University of Leeds.

Baker, P.A., Fritz, S.C., 2015. Nature and causes of Quaternary climate variation of tropical South America. Quat. Sci. Rev. 124, 31–47. https://doi.org/10.1016/j.quascirev.2015.06.011.

Baker, J.C.A., Gloor, M., Spracklen, D.V., Arnold, S.R., Tindall, J.C., Clerici, S.J., Leng, M. J., Brienen, R.J.W., 2016. What drives interannual variation in tree ring oxygen isotopes in the Amazon? Geophys. Res. Lett. 43, 11–831. https://doi.org/10.1002/2016GL071507.

Baker, J.C.A., Santos, G.M., Gloor, M., Brienen, R.J.W., 2017. Does Cedrela always form annual rings? Testing ring periodicity across South America using radiocarbon dating. Trees 31, 1999–2009. https://doi.org/10.1007/s00468-017-1604-9.

Baker, J.C.A., Gloor, M., Boom, A., Neill, D.A., Cintra, B.B.L., Clerici, S.J., Brienen, R.J. W., 2018. Questioning the Influence of Sunspots on Amazon Hydrology: even a Broken Clock Tells the right Time twice a Day. Geophys. Res. Lett. 45, 1419–1422. https://doi.org/10.1002/2017GL076889.

Bendix, J., Homeier, J., Cueva Ortiz, E., Emck, P., Breckle, S.-W., Richter, M., Beck, E., 2006a. Seasonality of weather and tree phenology in a tropical evergreen mountain rain forest. Int. J. Biometeorol. 50, 370–384. https://doi.org/10.1007/s00484-006-0029-8.

Bendix, J., Rollenbeck, R., Göttlicher, D., Cermak, J., 2006b. Cloud occurrence and cloud properties in Ecuador. Clim. Res. 30, 133–147. https://doi.org/10.3354/cr030133.

Bendix, J., Rollenbeck, R., Fabian, P., Emck, P., Richter, M., Beck, E., 2008. Climate variability. In: Gradients in a Tropical Mountain Ecosystem of Ecuador. Springer, pp. 281–290. https://doi.org/10.1007/978-3-540-73526-7_27.

Borella, S., Leuenberger, M., Saurer, M., Siegwolf, R., 1998. Reducing uncertainties in δ 13 C analysis of tree rings: pooling, milling, and cellulose extraction. J. Geophys. Res. Atmos. 103, 19519–19526. https://doi.org/10.1029/98JD01169.

Bräuning, A., Homeier, J., Cueva, E., Beck, E., Günter, S., 2008. Growth dynamics of trees in tropical mountain ecosystems. In: Gradients in a Tropical Mountain Ecosystem of Ecuador. Springer, pp. 291–302. https://doi.org/10.1007/978-3-540-73526-7_28.

Bräuning, A., Volland-Voigt, F., Burchardt, I., Ganzhi, O., Nauss, T., Peters, T., 2009. Climatic control of radial growth of Cedrela montana in a humid mountain rainforest in southern Ecuador. Erdkunde 63, 337–345. https://doi.org/10.3112/erdkunde.2009.04.04.

Brienen, R.J.W., Helle, G., Pons, T.L., Guyot, J.-L., Gloor, M., 2012. Oxygen isotopes in tree rings are a good proxy for Amazon precipitation and El Nino-Southern Oscillation variability. Proc. Natl. Acad. Sci. 109, 16957–16962. https://doi.org/10.1073/pnas.1205977109.

Bunn, A.G., 2008. A dendrochronology program library in R (dplR). Dendrochronologia 26, 115–124. https://doi.org/10.1016/j.dendro.2008.01.002.

Bunn, A.G., 2010. Statistical and visual crossdating in R using the dplR library. Dendrochronologia 28, 251–258. https://doi.org/10.1016/j.dendro.2009.12.001.

Buras, A., 2017. A comment on the expressed population signal. Dendrochronologia 44, 130–132. https://doi.org/10.1016/j.dendro.2017.03.005.

Cámara Artigas, R., Díaz del Olmo, F., 2013. Muestreo en transecto de formaciones vegetales de fanerófitos y caméfitos (I): fundamentos metodológicos. Estud. Geográficos 74, 67–88. https://doi.org/10.3989/estgeogr.201303.

Campelo, F., García-González, I., Nabais, C., 2012. detrendeR – a Graphical User Interface to process and visualize tree-ring data using R. Dendrochronologia 30, 57–60. https://doi.org/10.1016/j.dendro.2011.01.010.

Chao, W.C., Chen, B., 2001. The Origin of Monsoons. J. Atmos. Sci. 58, 3497–3507. https://doi.org/10.1175/1520-0469(2001)058<3497:TOOM>2.0.CO;2.

Cheng, H., Sinha, A., Cruz, F.W., Wang, X., Edwards, R.L., D'Horta, F.M., Ribas, C.C., Vuille, M., Stott, L.D., Auler, A.S., 2013. Climate change patterns in Amazonia and biodiversity. Nat. Commun. 4, 1411. https://doi.org/10.1038/ncomms2415.

CITES, (Convention on International Trade in Endangered Species of Wild Fauna and Flora), 2021. Appendices I, II and III.

Cook, E., Briffa, K., Shiyatov, S., Mazepa, V., Jones, P.D., 1990. Data analysis. In: Methods of Dendrochronology. Springer Netherlands, Dordrecht, pp. 97–162. https://doi.org/10.1007/978-94-015-7879-0_3.

Dee, D.P., Uppala, S.M., Simmons, A.J., Berrisford, P., Poli, P., Kobayashi, S., Andrae, U., Balmaseda, M.A., Balsamo, G., Bauer, P., Bechtold, P., Beljaars, A.C.M., van de

Berg, L., Bidlot, J., Bormann, N., Delsol, C., Dragani, R., Fuentes, M., Geer, A.J., Haimberger, L., Healy, S.B., Hersbach, H., Hólm, E.V., Isaksen, L., Kållberg, P., Köhler, M., Matricardi, M., McNally, A.P., Monge-Sanz, B.M., Morcrette, J.-J., Park, B.-K., Peubey, C., de Rosnay, P., Tavolato, C., Thépaut, J.-N., Vitart, F., 2011. The ERA-Interim reanalysis: configuration and performance of the data assimilation system. Q. J. R. Meteorol. Soc. 137, 553–597. https://doi.org/10.1002/qj.828.

Douville, H., Raghavan, K., Renwick, J., Allan, R.P., Arias, P.A., Barlow, M., Cerezo-Mota, R., Cherchi, A., Gan, T.Y., Gergis, J., Jiang, D., Khan, A., Pokam Mba, W., Rosenfeld, D., Tierney, J., Zolina, O., 2021. Water cycle changes. In: Climate Change 2021: The Physical Science Basis. Contribution of Working Group I to the Sixth Assessment Report of the Intergovernmental Panel on Climate Change.

Dünisch, O., Bauch, J., Gasparotto, L., 2002. Formation of increment zones and intraannual growth dynamics in the xylem of *Swietenia macrophylla*, *Carapa guianensis*, and *Cedrela odorata* (Meliaceae). IAWA J. 23, 101–119. https://doi.org/10.1163/22941932-90000292.

Engelmann, G., 1986. Instructions for the Collection and Preservation of Botanical Specimens. Ann. Missouri Bot. Gard. 73, 504. https://doi.org/10.2307/2399189.

Gagen, M., McCarroll, D., Loader, N.J., Robertson, I., 2011. Stable isotopes in dendroclimatology: moving beyond 'potential'. In: Dendroclimatology. Springer, pp. 147–172. https://doi.org/10.1007/978-1-4020-5725-0_6.

Garcia, O., 1985. Atlas of Highly Reflective Clouds for the Global Tropics: 1971–1985. Boulder, Colorado. https://psl.noaa.gov/data/dsets/hrc/.

García, N.O., 1994. South American climatology. Quat. Int. 21, 7–27. https://doi.org/10.1016/1040-6182(94)90018-3.

Garcia, S.R., Kayano, M.T., 2010. Some evidence on the relationship between the south American monsoon and the Atlantic ITCZ. Theor. Appl. Climatol. 99, 29–38. https://doi.org/10.1007/s00704-009-0107-z.

Garreaud, R.D., Vuille, M., Compagnucci, R., Marengo, J., 2009. Present-day south American climate. Palaeogeogr. Palaeoclimatol. Palaeoecol. 281, 180–195. https://doi.org/10.1016/j.palaeo.2007.10.032.

Gärtner, H., Schweingruber, F.H., 2013. Microscopic Preparation Techniques for Plant Stem Analysis. Kessel Publishing House, Remagen.

Grinsted, A., Moore, J.C., Jevrejeva, S., 2004. Application of the cross wavelet transform and wavelet coherence to geophysical time series. Nonlinear Process. Geophys. 11, 561–566. https://doi.org/10.5194/npg-11-561-2004.

Günter, S., Stimm, B., Cabrera, M., Diaz, M.L., Lojan, M., Ordoñez, E., Richter, M., Weber, M., 2008. Tree phenology in montane forests of southern Ecuador can be explained by precipitation, radiation and photoperiodic control. J. Trop. Ecol. 24, 247–258. https://doi.org/10.1017/S0266467408005063.

Harris, I., Osborn, T.J., Jones, P., Lister, D., 2020. Version 4 of the CRU TS monthly high-resolution gridded multivariate climate dataset. Sci. Data 7, 109. https://doi.org/10.1038/s41597-020-0453-3.

Hastenrath, S., 1997. Annual cycle of upper air circulation and convective activity over the tropical Americas. J. Geophys. Res. Atmos. 102, 4267–4274. https://doi.org/10.1029/96JD03122.

Hu, Y., Li, D., Liu, J., 2007. Abrupt seasonal variation of the ITCZ and the Hadley circulation. Geophys. Res. Lett. 34, L18814. https://doi.org/10.1029/2007GL030950.

Hua, Q., Barbetti, M., Rakowski, A.Z., 2013. Atmospheric Radiocarbon for the period 1950–2010. Radiocarbon 55, 2059–2072. https://doi.org/10.2458/azu_js_rc.v55i2.16177.

Ilbay-Yupa, M., Lavado-Casimiro, W., Rau, P., Zubieta, R., Castillón, F., 2021. Updating regionalization of precipitation in Ecuador. Theor. Appl. Climatol. 143, 1513–1528. https://doi.org/10.1007/s00704-020-03476-x.

Insel, N., Poulsen, C.J., Ehlers, T.A., 2010. Influence of the Andes Mountains on south American moisture transport, convection, and precipitation. Clim. Dyn. 35, 1477–1492. https://doi.org/10.1007/s00382-009-0637-1.

Janovics, R., Futó, I., Molnár, M., 2018. Sealed tube combustion method with MnO 2 for AMS 14 C measurement. Radiocarbon 60, 1347–1355. https://doi.org/10.1017/RDC.2018.110.

Jiménez-Sánchez, G., Markowski, P.M., Young, G.S., Stensrud, D.J., 2020. The orinoco low-level jet: an investigation of its mechanisms of formation using the WRF model. J. Geophys. Res. Atmos. 125, e2020JD032810 https://doi.org/10.1029/2020JD032810.

Kéri, M., Palcsu, L., Túri, M., Heim, E., Czébely, A., Novák, L., Bányai, I., 2015. 13C NMR analysis of cellulose samples from different preparation methods. Cellulose 22, 2211–2220. https://doi.org/10.1007/s10570-015-0642-y.

Koecke, A.V., Muellner-Riehl, A.N., Pennington, T.D., Schorr, G., Schnitzler, J., 2013. Niche evolution through time and across continents: the story of Neotropical Cedrela (Meliaceae). Am. J. Bot. 100, 1800–1810. https://doi.org/10.3732/ajb.1300059.

Kurita, N., Ichiyanagi, K., Matsumoto, J., Yamanaka, M.D., Ohata, T., 2009. The relationship between the isotopic content of precipitation and the precipitation amount in tropical regions. J. Geochem. Explor. 102, 113–122. https://doi.org/10.1016/j.gexplo.2009.03.002.

Layme-Huaman, E.T., Ferrero, M.E., Palacios-Lazaro, K.S., Requena-Rojas, E.J., 2018. Cedrela nebulosa: a novel species for dendroclimatological studies in the montane tropics of South America. Dendrochronologia 50, 105–112. https://doi.org/10.1016/j.dendro.2018.06.004.

Loader, N.J., McCarroll, D., Gagen, M., Robertson, I., Jalkanen, R., 2007. Extracting climatic information from stable isotopes in tree rings. In: Terrestrial Ecology. Elsevier, pp. 25–48. https://doi.org/10.1016/S1936-7961(07)01003-2.

Managave, S.R., Ramesh, R., 2012. Isotope dendroclimatology: a review with a special emphasis on tropics. In: Earth System Science Data Discussions. Copernicus GmbH, pp. 811–833. https://doi.org/10.1007/978-3-642-10637-8_38.

Marengo, J.A., Liebmann, B., Grimm, A.M., Misra, V., Silva Dias, P.L., Cavalcanti, I.F.A., Carvalho, L.M.V., Berbery, E.H., Ambrizzi, T., Vera, C.S., Saulo, A.C., Nogues-Paegle, J., Zipser, E., Seth, A., Alves, L.M., 2012. Recent developments on the south American monsoon system. Int. J. Climatol. 32, 1–21. https://doi.org/10.1002/joc.2254.

McCarroll, D., Loader, N.J., 2004. Stable isotopes in tree rings. Quat. Sci. Rev. 23, 771–801. https://doi.org/10.1016/j.quascirev.2003.06.017.

Meko, D.M., Touchan, R., Anchukaitis, K.J., 2011. Seascorr: a MATLAB program for identifying the seasonal climate signal in an annual tree-ring time series. Comput. Geosci. 37, 1234–1241. https://doi.org/10.1016/j.cageo.2011.01.013.

Molnár, M., Janovics, R., Major, I., Orsovszki, J., Gönczi, R., Veres, M., Leonard, A.G., Castle, S.M., Lange, T.E., Wacker, L., Hajdas, I., Julll, A.J.T., 2013a. Status report of the new AMS 14C sample preparation lab of the hertelendi laboratory of environmental studies (Debrecen, Hungary). Radiocarbon 55, 665–676. https://doi.org/10.2458/azu_js_rc.55.16394.

Molnár, M., Rinyu, L., Veres, M., Seiler, M., Wacker, L., Synal, H.-A., 2013b. EnvironMICADAS: a mini 14 C AMS with enhanced gas ion source interface in the hertelendi laboratory of environmental Studies (HEKAL), Hungary. Radiocarbon 55, 338–344. https://doi.org/10.1017/S0033822200057453.

Montoya, E., Keen, H.F., Luzuriaga, C.X., Gosling, W.D., 2018. Long-term vegetation dynamics in a megadiverse hotspot: the ice-age record of a pre-montane forest of Central Ecuador. Front. Plant Sci. 9, 1–14. https://doi.org/10.3389/fpls.2018.00196.

Mosblech, N.A.S., Bush, M.B., Gosling, W.D., Hodell, D., Thomas, L., van Calsteren, P., Correa-Metrio, A., Valencia, B.G., Curtis, J., van Woesik, R., 2012. North Atlantic forcing of Amazonian precipitation during the last ice age. Nat. Geosci. 5, 817–820. https://doi.org/10.1038/ngeo1588.

Murakami, T., Nakazawa, T., 1985. Transition from the Southern to Northern Hemisphere Summer Monsoon. Mon. Weather Rev. 113, 1470–1486. https://doi.org/10.1175/1520-0493(1985)113<1470:TFTSTN>2.0.CO;2.

Nacimba, M., 2015. Crecimiento y Dendrocronología de Cedrela Odorata en un bosque de la Amazonía Ecuatoriana. Pontificia Universidad Católica del Ecuador. http://repositorio.puce.edu.ec/bitstream/handle/22000/9661/Tesis%20Mayra%20Nacimba.pdf?sequence=1.

Neill, D., Guevara, J., 2013. Sistema de Clasificación De Ecosistemas del Ecuador Continental. In: Ministerio del Ambiente del Ecuador (Ed.), Sistema de Clasificación De Ecosistemas Del Ecuador Continental. Quito, pp. 190–192.

NOAA, 1994. NCEP/NCAR Global Reanalysis Products, 1948-Continuing.

Pennington, T.D., Muellner, A.N., 2010. A Monograph of Cedrela (Meliaceae). DH Books, Sherborne, UK.

Poveda, G., Waylen, P.R., Pulwarty, R.S., 2006. Annual and inter-annual variability of the present climate in northern South America and southern Mesoamerica. Palaeogeogr. Palaeoclimatol. Palaeoecol. 234, 3–27. https://doi.org/10.1016/j.palaeo.2005.10.031.

Poveda, G., Jaramillo, L., Vallejo, L.F., 2014. Seasonal precipitation patterns along pathways of South American low-level jets and aerial rivers. Water Resour. Res. 50, 98–118. https://doi.org/10.1002/2013WR014087.

Pucha-Cofrep, D., Peters, T., Bräuning, A., 2015. Wet season precipitation during the past century reconstructed from tree-rings of a tropical dry forest in Southern Ecuador. Glob. Planet. Chang. 133, 65–78. https://doi.org/10.1016/j.gloplacha.2015.08.003.

R Core Team, 2020. R: A Language and Environment for Statistical Computing.

Raia, A., Cavalcanti, I.F.A., 2008. The Life Cycle of the South American Monsoon System. J. Clim. 21, 6227–6246. https://doi.org/10.1175/2008JCLI2249.1.

Reimer, P.J., Reimer, R., 2004. CALIBomb radiocarbon calibration. In: Interact. Progr.. Available on-line. http://intcal.qub.ac.uk/CALIBomb/frameset.html.

Rinn, F., 2012. TSAPWin Scientific: Time Series Analysis and Presentation for Dendrochronology and Related Applications.

Rinyu, L., Molnár, M., Major, I., Nagy, T., Veres, M., Kimák, Á., Wacker, L., Synal, H.-A., 2013. Optimization of sealed tube graphitization method for environmental C-14 Studies using MICADAS. Nucl. Instrum. Methods Phys. Res. Sect. B Beam Interact. Mater. Atoms 294, 270–275. https://doi.org/10.1016/j.nimb.2012.08.042.

Rohde, R.A., Hausfather, Z., 2020. The Berkeley earth land/ocean temperature record. Earth Syst. Sci. Data 12, 3469–3479. https://doi.org/10.5194/essd-12-3469-2020.

Saurer, M., Robertson, I., Siegwolf, R., Leuenberger, M., 1998. Oxygen isotope analysis of cellulose: an interlaboratory comparison. Anal. Chem. 70, 2074–2080. https://doi.org/10.1021/ac971022f.

Schneider, T., Bischoff, T., Haug, G.H., 2014. Migrations and dynamics of the intertropical convergence zone. Nature 513, 45–53. https://doi.org/10.1038/nature13636.

Stahle, D.W., 1999. Useful strategies for the development of tropical tree-ring chronologies. IAWA J. 20, 249–253. https://doi.org/10.1163/22941932-90000688.

Stokes, M.A., Smiley, T.L., 1968. An Introduction to Tree-Ring Dating. University of Chicago Press, Chicago, IL.

Tans, P., Keeling, R., 2020. NOAA/GML Trends in Atmospheric Carbon Dioxide [WWW Document]. URL. https://www.esrl.noaa.gov/gmd/ccgg/trends/data.html (accessed 3.15.21).

Treydte, K., Boda, S., Graf Pannatier, E., Fonti, P., Frank, D., Ullrich, B., Saurer, M., Siegwolf, R., Battipaglia, G., Werner, W., Gessler, A., 2014. Seasonal transfer of oxygen isotopes from precipitation and soil to the tree ring: source water versus needle water enrichment. New Phytol. 202, 772–783. https://doi.org/10.1111/nph.12741.

Tropicos.org, 2020. https://www.tropicos.org/home.

Trouet, V., Van Oldenborgh, G.J., 2013. KNMI climate explorer: a web-based research tool for high-resolution paleoclimatology. Tree-Ring Res. 69, 3–13. https://doi.org/10.3959/1536-1098-69.1.3.

Túri, M., Hubay, K., Molnár, M., Braun, M., László, E., Futó, I., Palcsu, L., 2021. Holocene paleoclimate reconstruction based on stable isotope results of Sphagnum cellulose,

Mohos peat bog, Romania. J. Paleolimnol. 66, 229–248. https://doi.org/10.1007/s10933-021-00202-z.
van der Sleen, P., Zuidema, P.A., Pons, T.L., 2017. Stable isotopes in tropical tree rings: theory, methods and applications. Funct. Ecol. 31, 1674–1689. https://doi.org/10.1111/1365-2435.12889.
Villacís, M., Vimeux, F., Taupin, J.D., 2008. Analysis of the climate controls on the isotopic composition of precipitation (δ18O) at Nuevo Rocafuerte, 74.5°W, 0.9°S, 250 m, Ecuador. Compt. Rendus Geosci. 340, 1–9. https://doi.org/10.1016/j.crte.2007.11.003.
Vimeux, F., Gallaire, R., Bony, S., Hoffmann, G., Chiang, J.C.H., 2005. What are the climate controls on δD in precipitation in the Zongo Valley (Bolivia)? Implications for the Illimani ice core interpretation. Earth Planet. Sci. Lett. 240, 205–220. https://doi.org/10.1016/j.epsl.2005.09.031.
Volland, F., Pucha, D., Bräuning, A., 2015. Hydro-climatic variability in southern Ecuador reflected by tree-ring oxygen isotopes. Erdkunde 70, 69–82. https://doi.org/10.3112/erdkunde.2016.01.05.
Vuille, M., Bradley, R.S., Keimig, F., 2000. Climate Variability in the Andes of Ecuador and its Relation to Tropical Pacific and Atlantic Sea Surface Temperature Anomalies. J. Clim. 13, 2520–2535. https://doi.org/10.1175/1520-0442(2000)013<2520:CVITAO>2.0.CO;2.
Vuille, M., Bradley, R.S., Werner, M., Healy, R., Keimig, F., 2003. Modeling δ18O in precipitation over the tropical Americas: 1. Interannual variability and climatic controls. J. Geophys. Res. Atmos. 108 https://doi.org/10.1029/2001JD002038.
Vuille, M., Burns, S.J., Taylor, B.L., Cruz, F.W., Bird, B.W., Abbott, M.B., Kanner, L.C., Cheng, H., Novello, V.F., 2012. A review of the south American monsoon history as recorded in stable isotopic proxies over the past two millennia. Clim. Past 8, 1309–1321. https://doi.org/10.5194/cp-8-1309-2012.
Waliser, D.E., Jiang, X., 2015. Intertropical convergence zone. In: Encyclopedia of Atmospheric Sciences. Elsevier, pp. 121–131. https://doi.org/10.1016/B978-0-12-382225-3.00417-5.
Wang, H., Fu, R., 2002. Cross-equatorial flow and seasonal cycle of precipitation over South America. J. Clim. 15, 1591–1608. https://doi.org/10.1175/1520-0442(2002)015<1591:CEFASC>2.0.CO;2.
Wang, B., Liu, J., Kim, H.-J., Webster, P.J., Yim, S.-Y., Xiang, B., 2013. Northern Hemisphere summer monsoon intensified by mega-El Nino/southern oscillation and Atlantic multidecadal oscillation. Proc. Natl. Acad. Sci. 110, 5347–5352. https://doi.org/10.1073/pnas.1219405110.
Warner, M.S.C., 2018. Introduction to PySPLIT: a Python toolkit for NOAA ARL's HYSPLIT Model. Comput. Sci. Eng. 20, 47–62. https://doi.org/10.1109/MCSE.2017.3301549.
Wigley, T.M.L., Briffa, K.R., Jones, P.D., 1984. On the average value of correlated time series with applications in dendroclimatology and hydrometeorology. J. Clim. Appl. Meteorol. https://doi.org/10.1175/1520-0450(1984)023<0201:OTAVOC>2.0.CO;2.
Xian, P., Miller, R.L., 2008. Abrupt seasonal migration of the ITCZ into the summer hemisphere. J. Atmos. Sci. 65, 1878–1895. https://doi.org/10.1175/2007JAS2367.1.
Yoon, J.-H., Zeng, N., 2010. An Atlantic influence on Amazon rainfall. Clim. Dyn. 34, 249–264. https://doi.org/10.1007/s00382-009-0551-6.
Zhou, J., Lau, K.-M., 1998. Does a monsoon climate exist over South America? J. Clim. 11, 1020–1040. https://doi.org/10.1175/1520-0442(1998)011<1020:DAMCEO>2.0.CO;2.